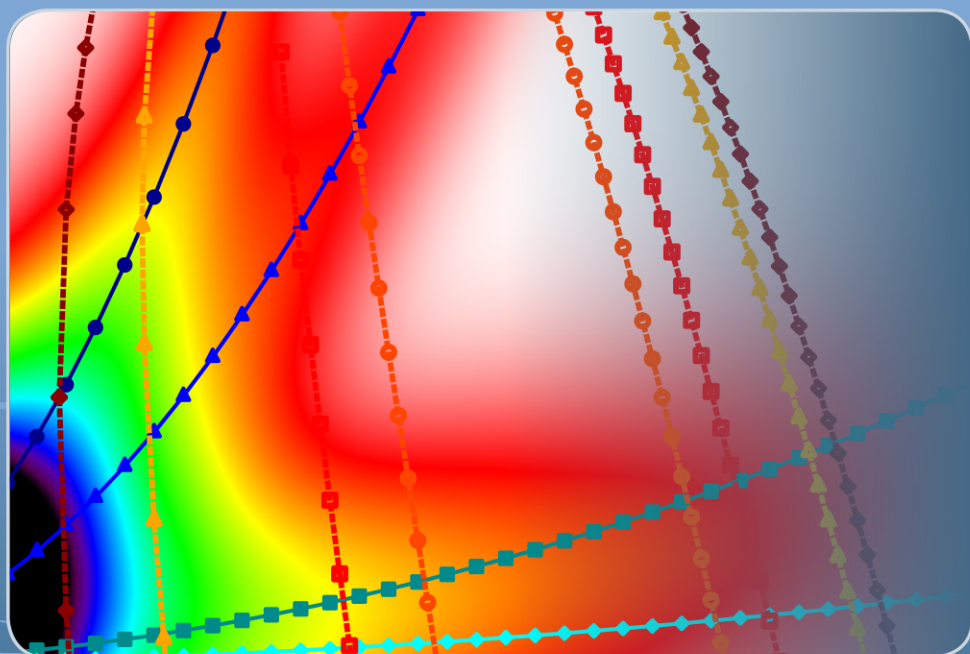


# La Rivista del Nuovo Cimento *della Società Italiana di Fisica*

Experimental studies of nuclear quantum effects  
in condensed matter: the case of water

C. ANDREANI, R. SENESI, M. KRZYSTYNIAK,  
G. ROMANELLI AND F. FERNANDEZ-ALONSO



## Experimental studies of nuclear quantum effects in condensed matter: the case of water

C. ANDREANI<sup>(1)(2)(3)</sup>, R. SENESI<sup>(1)(2)(3)</sup>, M. KRZYSTYNIAK<sup>(4)(5)</sup>, G. ROMANELLI<sup>(4)</sup>  
and F. FERNANDEZ-ALONSO<sup>(4)(6)</sup>

<sup>(1)</sup> *Dipartimento di Fisica, Università degli Studi di Roma "Tor Vergata" and  
Dipartimento di Fisica and Centro NAST, Via della Ricerca Scientifica 1  
00133 Roma, Italy*

<sup>(2)</sup> *Consiglio Nazionale delle Ricerche, CNR-IPCF, Sezione di Messina  
98122, Messina, Italy*

<sup>(3)</sup> *Museo Storico della Fisica e Centro Studi e Ricerche Enrico Fermi - 00184 Roma, Italy*

<sup>(4)</sup> *ISIS Facility, Rutherford Appleton Laboratory, Chilton, Didcot  
Oxfordshire OX11 0QX, UK*

<sup>(5)</sup> *School of Science and Technology, Nottingham Trent University, Clifton Campus  
Nottingham, NG11 8NS, UK*

<sup>(6)</sup> *Department of Physics and Astronomy, University College London  
Gower Street, London WC1E 6BT, UK*

received 7 February 2018

**Summary.** — Water continues to be the focus of a considerable number of experimental and theoretical investigations because of the important role it plays in many phenomena in fundamental and applied science, as well as its biological and technological importance. The ability of water to create a three-dimensional network of hydrogen bonds makes this molecule uniquely versatile. Atoms in water display characteristic mean kinetic energies well above the thermodynamic temperature of the system, as opposed to the celebrated case of a perfect gas of non-interacting particles. Nuclear quantum effects have a profound influence on the structure and dynamics of hydrogen-bonded systems, such as water. These effects are reflected in the underlying nuclear momentum distributions, experimentally accessible using electron-volt neutron spectroscopy at pulsed spallation neutron sources, with a technique known as deep inelastic neutron scattering. In this topical review, the technique is discussed along with the conceptual framework and several case studies that bring to the fore the role of nuclear quantum effects in describing water. These state-of-the-art measurements are also benchmarked against theoretical predictions using path-integral molecular dynamics. We close by discussing and highlighting current challenges and future opportunities in this thriving area of condensed-matter research.

---

|    |        |   |
|----|--------|---|
| 2  | 1.     | Introduction  |
| 5  | 2.     | Deep inelastic neutron scattering                                   |
| 5  | 2'1.   | The impulse approximation and the neutron Compton profile           |
| 10 | 2'2.   | Validity of the impulse approximation and corrections at finite $Q$ |
| 13 | 2'3.   | Extracting momentum distributions and mean kinetic energies         |
| 15 | 2'4.   | Nuclear momentum distributions in the harmonic approximation        |
| 15 | 2'5.   | The physical origin of nuclear momentum distributions               |
| 20 | 2'6.   | Performing a DINS measurement                                       |
| 20 | 2'6.1. | The measurement of neutron Compton profiles                         |
| 25 | 2'6.2. | Experimental resolution and fitting procedure                       |
| 26 | 3.     | Atomic quantum dynamics in water, ice and amorphous ices            |
| 30 | 3'1.   | Water across the melting point                                      |
| 32 | 3'2.   | The triple point of water   |
| 33 | 3'3.   | Water under supercritical conditions                                |
| 37 | 3'4.   | Heavy water and quantum melting                                     |
| 38 | 3'5.   | Amorphous ices  |
| 41 | 4.     | Outlook and future directions                                       |
| 43 |        | References  |

---

## 1. – Introduction

Although water is a small triatomic molecule with a simple stoichiometry, it is still at the centre of scientific investigations because of the elusive description of its structure and dynamics in its condensed phases [1]. One of the most important ingredients of such a description is the need to consider its constituent nuclei as truly quantum particles. A direct consequence of this description is the introduction of nuclear quantum effects (NQE), such as those arising from isotopic substitution or the intrinsic zero-point energy (ZPE) associated with the spatial confinement of nuclei. Isotope effects in light ( $\text{H}_2\text{O}$ ) and heavy water ( $\text{D}_2\text{O}$ ) [2] have been considered as responsible, for example, for the mild temperature dependence of the structural relaxation in supercooled water [3], or for the emergence of glassy transitions and crystallisation [4]. Moreover, NQEs have been shown to have significant effects on the structure of proteins in aqueous media [5], and on the equilibrium fractionation ratios of hydrogen isotopologs [6]. From a conceptual viewpoint, ZPEs may be viewed as arising primarily from strong chemical forces, and are affected by the anisotropy and the anharmonicity of the local potential around the atom, that can be both of an inter- or intramolecular nature. NQEs manifest themselves as a marked broadening of the nuclear momentum distribution (NMD), a result that is at odds with the predictions of the statistical theory by Maxwell and Boltzmann (MB), whereby the width of the NMD, as well as its associated mean kinetic energy,  $\langle E_K \rangle$ , remain always proportional to the thermodynamic temperature of the system,  $T$ , *i.e.*,  $\langle E_K \rangle \sim k_B T$ , where  $k_B$  is Boltzmann's constant. To illustrate these notions, fig. 1 shows the case of the hydrogen NMD in ice at 271 K. From these data, one can appreciate how the prediction from classical statistical mechanics is rather inadequate, as the effective temperature for the hydrogen dynamics should be increased by about  $\sim 880$  K. Moreover, a simple scaling of the thermodynamic temperature would still miss essential physics related to the anisotropy of the NMD and the associated anharmonicity of the underlying potential-energy landscape. All proton NMDs in liquid water, ice, or around

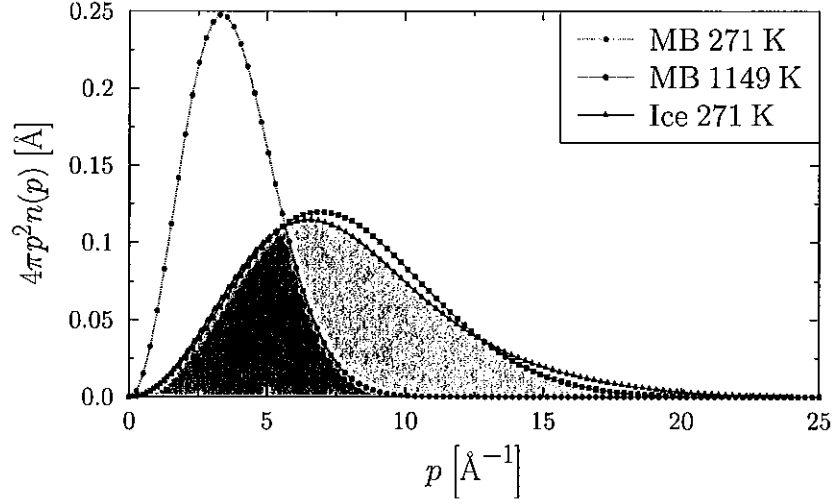


Fig. 1. – Spherically averaged proton NMDs for ice at  $T = 271$  K (black) and an MB distribution at the same temperature (blue). The red trace corresponds to an MB distribution at a much higher temperature of  $T = 1149$  K, chosen to approach the experimental data shown in black [93].

biological molecules deviate dramatically from the aforementioned MB predictions, a fact that should not be surprising if we consider that typical vibrational frequencies associated with intramolecular stretching and bending motions in water are of the order of hundreds of meV, *i.e.*, significantly higher than  $k_B T$  at room temperature [7, 8]. In this sense, the intrinsic broadening of the NMD provides a means of measuring an effective “quantum temperature” around a given atom, which can deviate enormously from the thermodynamic (macroscopic) temperature of the system. The need for a quantum description of nuclear dynamics in condensed matter has also triggered exciting developments in computer simulations [9-19] largely based on the path-integral formalism of Feynman [20, 21], where nuclei are delocalised in both position and momentum from the outset.

Neutron scattering has been extensively employed to study hydrogen-containing materials, taking advantage of the large total neutron-scattering cross section from protons, and the possibility to separate coherent from incoherent scattering, as well as elastic and inelastic events [22]. Numerous studies have investigated the structure of liquids using neutron diffraction [23-27], or vibrational features using (primarily incoherent) neutron spectroscopy [28]. Both techniques have photon-based analogues, including X-ray diffraction, infrared, and Raman scattering. When the energy transferred by the neutron is higher than a few electronvolts, the scattering can be completely ascribed to the dynamics of single nuclei, a regime referred to as deep inelastic neutron scattering (DINS) [29-33]. The interpretation of DINS data relies essentially on the fact that, provided that the momentum  $\hbar\mathbf{Q}$  transferred between the incident neutron and the target system is sufficiently high, the neutron scattering response provides a direct measurement of NMDs, as well as the nuclear mean kinetic energy,  $\langle E_K \rangle$ . DINS experiments rely on the use of high-energy (so called “epithermal”) neutrons with energies in the eV range [34], only available at pulsed neutron sources, such as the ISIS Facility [35], Rutherford Appleton Laboratory, United Kingdom. Reviews of the

use of electronvolt neutron spectroscopy to interrogate the properties of condensed-matter systems across physics, chemistry, biology, and materials science can be found in refs. [31-33].

At present, the VESUVIO spectrometer [36-39] at ISIS is the flagship instrument for electronvolt neutron spectroscopy. This unique spectrometer is the newest incarnation of the previous eV Spectrometer (eVS) [31, 40, 41]. As such, VESUVIO constitutes a tantalising example of continuous evolution in technique development over the past decade [42-63]. Early DINS investigations using this instrumentation focused on a broad range of light atoms and molecules, both in the bulk and in confined geometries, and over a broad range of physico-chemical conditions. These include hydrogen-bonded systems [64], metal hydrides [65-68], catalysts [69], glasses [70, 71], amorphous and metastable matter [72], as well as quantum fluids and solids [73-83] —for DINS work on  $^4\text{He}$  see, in particular, refs. [76, 84, 85]; for fluid molecular hydrogen and deuterium, see refs. [86-88].

Over the past decade, the experimental programme on VESUVIO has experienced a paradigm shift primarily along two directions: first, an increasing interest in the exploration of NQEs for atoms heavier than hydrogen, such as those found in lithium hydride [89], hydrogen fluoride [90], lithium fluoride [91], or heavy water [92]; second, the expansion of capabilities via the concurrent implementation of neutron transmission and diffraction over a wide dynamic range. In this latter case, systems that have been tackled include: bulk water and ice [93-95]; confined water in carbon-based materials [96] and [97]; geological specimens [98]; solid-state polymorphs [99]; as well as materials of direct technological relevance such as solid acids for fuel cells [100], metallic alloys for nuclear applications [101], or dental cements [102]. We also note that there have been parallel and exciting developments of novel concepts and devices using epithermal neutrons for specific applications that transcend the scope of this review. In some cases, these new techniques have gone beyond their exclusive use for DINS. Examples include investigations of archaeological artefacts and cultural heritage [103-105], or the irradiation of electronic components [106, 107].

The primary purpose of this review is to provide a self-contained account of experimental efforts to date to probe NQEs in water-based systems using DINS. To set the scene, sect. 2 provides a succinct account of the theoretical framework to interpret DINS data: sects. 2.1 and 2.2 introduce the celebrated impulse approximation (IA) [40, 108]; sect. 2.3 discusses how to extract NMDs and mean kinetic energies; analytic representations of NMDs within the harmonic approximation are introduced in sect. 2.4, whereas sect. 2.5 discusses how NMDs may be related to the chemical environment around a given atom; and sect. 2.6 gives a number of guidelines to perform successful DINS experiments. Section 3 presents the most recent examples of DINS work on water-based media, including a critical comparison with state-of-the-art simulations using *ab initio* path-integral molecular dynamics [109, 110]. These studies include: H, D and O NMDs in the bulk and in confined geometries; crystalline [93, 109] and amorphous ices [94, 111]; water in the supercritical state [110, 112, 113]; and supercooled water [95]. In the particular case of melting, we describe how the emergence of competing quantum effects dictates the phase behaviour of the liquid. This particular case also represents a timely example of the combined use of DINS and INS experiments, along with the most sophisticated approaches to computational materials modelling available at present. Section 4 concludes this review with a discussion of present-day theoretical and experimental challenges, as well as envisaged technique developments on the horizon.

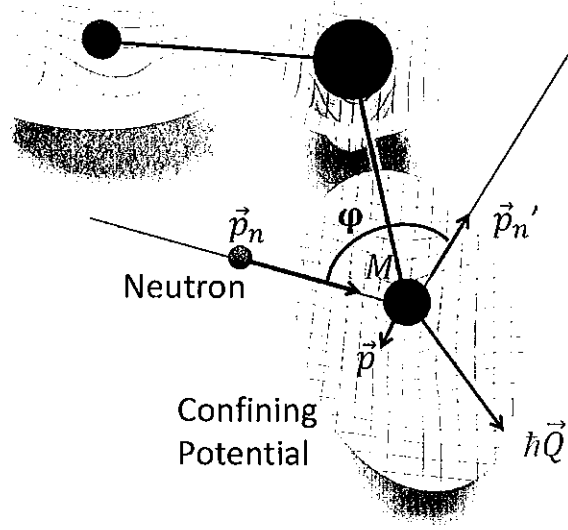


Fig. 2. – Illustration of the kinematic variables used in the main text to describe the scattering of eV neutrons in a condensed matter system: the curved grid represents the confining potential around a given atom in a lattice.

## 2. – Deep inelastic neutron scattering

2.1. *The impulse approximation and the neutron Compton profile.* – DINS refers to a neutron-scattering regime where the energy of the incident neutron is well above the binding energies of the scattering nuclei. This condition implies large momentum,  $\hbar Q$ , and energy  $\hbar\omega$  transfers in the scattering process, relative to other momentum and energy scales of the nuclei composing the system under investigation [31, 32, 40, 114, 115].

This neutron scattering regime is well described within the framework of the so-called IA, which is exact in the limit of infinite momentum transfer [40, 114, 115]. The IA assumes that in a scattering process, a single particle of the system is struck by the probe, and that particle recoils freely from the collision with negligible interparticle interaction in the final state, *i.e.*, the wave function of the particle in its final state is a plane wave. Let us suppose that a neutron of momentum  $\mathbf{p}_n$  is scattered by an atom with momentum  $\mathbf{p}$ . Then, applying momentum and energy conservation, the quantities  $\hbar Q$  and  $\hbar\omega$  are related by the following expression:

$$(1) \quad \hbar\omega = \frac{(\mathbf{p}_n - \mathbf{p}'_n)^2}{2M} + \frac{(\mathbf{p}_n - \mathbf{p}'_n) \cdot \mathbf{p}}{M} = \frac{\hbar^2 Q^2}{2M} + \frac{\mathbf{Q} \cdot \mathbf{p}}{M},$$

where  $\hbar Q = \mathbf{p}_n - \mathbf{p}'_n$ , with  $\mathbf{p}_n$  and  $\mathbf{p}'_n$  are the momenta of the incident and scattered neutron,  $M$  and  $\mathbf{p}$  are the mass and the momentum of struck particle before collision. In eq. (1),  $\frac{\hbar^2 Q^2}{2M}$  is the free recoil energy of the nucleus,  $\hbar\omega_r$ , also labelled as  $E_r$ . It represents the kinetic energy the struck nucleus would have if it were stationary and able to absorb all the momentum transferred by the neutron. These kinematic variables

are shown pictorially in fig. 2, for the case of the scattering of a neutron from a water molecule, with  $\phi$  being the scattering angle. In this context, we will see below that the energy distribution of the scattered neutrons can be directly related to the distribution of particle momenta parallel to the wave vector transfer.

The probability of a neutron scattering off a nucleus, the scattering cross section  $\sigma = 4\pi b^2$ , is proportional to the square of the scattering length,  $b$ , a parameter dependent upon the nuclear isotope and its spin. For a sample with a single atomic species investigated with unpolarised neutrons, one needs to consider the average, denoted as  $\langle \dots \rangle$ , of the scattering length over all possible isotopes and spins [116]

$$(2) \quad \sigma = 4\pi \langle b^2 \rangle = 4\pi \langle b \rangle^2 + 4\pi (\langle b^2 \rangle - \langle b \rangle^2) = \sigma_c + \sigma_i,$$

where the convenient distinction between the coherent and incoherent contributions to the scattering cross section,  $\sigma_c$  and  $\sigma_i$  respectively, has been made. In this way, the double differential neutron-scattering cross section for a single atomic species for a beam of unpolarized neutrons is related to the dynamic structure factor  $S(\mathbf{Q}, \omega)$  via the relation [32, 117, 118]

$$(3) \quad \frac{d^2\sigma(E_0, E_1, \phi)}{d\Omega dE_1} = \hbar^{-1} \sqrt{\frac{E_1}{E_0}} \frac{\sigma}{4\pi} S(\mathbf{Q}, \omega) = \hbar^{-1} \sqrt{\frac{E_1}{E_0}} [\sigma_c S(\mathbf{Q}, \omega) + \sigma_i S_I(\mathbf{Q}, \omega)],$$

where  $E_0$  is the energy of the incident neutron, and  $E_1$  is the energy of the scattered neutron. Scattering takes place within a solid angle between  $\Omega$  and  $\Omega + d\Omega$  with final energies between  $E_1$  and  $E_1 + dE_1$ .

$S(\mathbf{Q}, \omega)$  and  $S_I(\mathbf{Q}, \omega)$  can then be expressed in terms of the two-particle correlation function  $Y_{jj'}(\mathbf{Q}, t)$  and the single-particle correlation function  $Y_{jj}(\mathbf{Q}, t)$ , respectively [31, 32, 118]:

$$(4) \quad S(\mathbf{Q}, \omega) = \frac{1}{2\pi N} \int_{-\infty}^{\infty} \exp(i\omega t) \sum_{jj'} Y_{jj'}(\mathbf{Q}, t) dt$$

and

$$(5) \quad S_I(\mathbf{Q}, \omega) = \frac{1}{2\pi N} \int_{-\infty}^{\infty} \exp(i\omega t) \sum_j Y_{jj}(\mathbf{Q}, t) dt,$$

where  $N$  is the number of nuclei in the target system and  $Y_{jj'}(\mathbf{Q}, t)$  and  $Y_{jj}(\mathbf{Q}, t)$  yield, respectively,

$$(6) \quad Y_{jj'}(\mathbf{Q}, t) = \langle \exp[-i\mathbf{Q} \cdot \hat{\mathbf{r}}_j] \exp[i\mathbf{Q} \cdot \hat{\mathbf{r}}_{j'}(t)] \rangle$$

and

$$(7) \quad Y_{jj}(\mathbf{Q}, t) = \langle \exp[-i\mathbf{Q} \cdot \hat{\mathbf{r}}_j] \exp[i\mathbf{Q} \cdot \hat{\mathbf{r}}_j(t)] \rangle,$$

where the  $\langle \dots \rangle$  denotes the thermal ensemble average. Here  $\hat{\mathbf{r}}_j(t)$  is the Heisenberg operator denoting the position of nucleus  $j$  at time  $t$ ,  $\hat{\mathbf{r}}_j = \hat{\mathbf{r}}_j(0)$  and the operator  $\exp[i\mathbf{Q} \cdot \hat{\mathbf{r}}_j]$  couples the plane wave of the neutron with the position of the nucleus in the

target system. The key approximation used in eqs. (6) and (7) is that, provided that  $t$  is sufficiently small,  $\hat{\mathbf{r}}_j(t)$  can be replaced by [33]

$$(8) \quad \hat{\mathbf{r}}_j(t) \simeq \hat{\mathbf{r}}_j + \frac{t}{M_j} \hat{\mathbf{p}}_j,$$

where  $\hat{\mathbf{p}}_j$  is the momentum operator and  $M_j$  the mass of nucleus  $j$ . The approximation in eq. (8) leads to

$$(9) \quad Y_{jj'}(\mathbf{Q}, t) = \exp \left[ \frac{i\hbar t Q^2}{2M_j} \delta_{jj'} \right] \left\langle \exp \left[ -i\mathbf{Q} \cdot (\hat{\mathbf{r}}_{j'} - \hat{\mathbf{r}}_j) + \frac{it}{M_{j'}} \mathbf{Q} \cdot \hat{\mathbf{p}}_{j'} \right] \right\rangle.$$

In the limit of large  $\hbar Q$ , only terms with  $j = j'$  are retained and eq. (9) reads

$$(10) \quad Y_{jj}(\mathbf{Q}, t) = \exp \left[ \frac{i\hbar t Q^2}{2M_j} \right] \left\langle \exp \left[ \frac{it}{M_j} \mathbf{Q} \cdot \hat{\mathbf{p}}_j \right] \right\rangle.$$

From eqs. (9) and (10),  $S_I(\mathbf{Q}, E)$  can be written as

$$(11) \quad S_I(\mathbf{Q}, \omega) = \frac{1}{2\pi N} \sum_j \int_{-\infty}^{\infty} \exp \left[ \frac{i\omega t}{\hbar} + \frac{i\hbar t Q^2}{2M} \right] \left\langle \exp \left[ \frac{it}{M} \mathbf{Q} \cdot \hat{\mathbf{p}}_j \right] \right\rangle dt,$$

where evaluation of the correlation function  $\langle \dots \rangle$  in eq. (11) leads to the formal definition of the NMD,  $n(\mathbf{p})$ , that is

$$(12) \quad \left\langle \exp \left[ \frac{it}{M} \mathbf{Q} \cdot \hat{\mathbf{p}}_j \right] \right\rangle = \int n(\mathbf{p}) \exp \left[ \frac{it}{M} \mathbf{Q} \cdot \mathbf{p} \right] d\mathbf{p}.$$

Within the IA,  $S_I(\mathbf{Q}, \omega)$  for an isotropic system may be obtained by using eq. (12) in eq. (11), and performing the temporal integral

$$(13) \quad S_{IA}(\mathbf{Q}, \omega) = \hbar \int n(\mathbf{p}) \delta \left[ \hbar\omega - \hbar\omega_r - \frac{\mathbf{p} \cdot \hbar\mathbf{Q}}{M} \right] d\mathbf{p}.$$

In eq. (13), the term  $\mathbf{p} \cdot \hbar\mathbf{Q}$  represents the projection of the NMD along the direction of  $\mathbf{Q}$ , leading to a broadening of the energy distribution of scattered neutrons, akin to the Doppler effect. We recall that the traditional formalism based on a formal definition of the Debye-Waller factor along with the quantisation of excitations customarily used in the description of INS spectra relies on small values of the product between momentum transfer and mean-square displacements, so as to allow for a Taylor series describing elastic, one-phonon, and higher-order multi-phonon events. This approach is not convenient in the DINS regime because of the large values of  $Q$  involved, whereby the neutron excites all possible modes of the system. The equivalence between these two approaches has been discussed in, for example, ref. [115].

For a single nucleus,  $n(\mathbf{p})$  is expressed by

$$(14) \quad n(\mathbf{p}) = |\Phi(\mathbf{p})|^2 = \left| \frac{1}{\sqrt{8\pi^3}} \int \exp \left[ \frac{i\mathbf{p} \cdot \mathbf{x}}{\hbar} \right] \Psi(\mathbf{x}) d\mathbf{x} \right|^2.$$



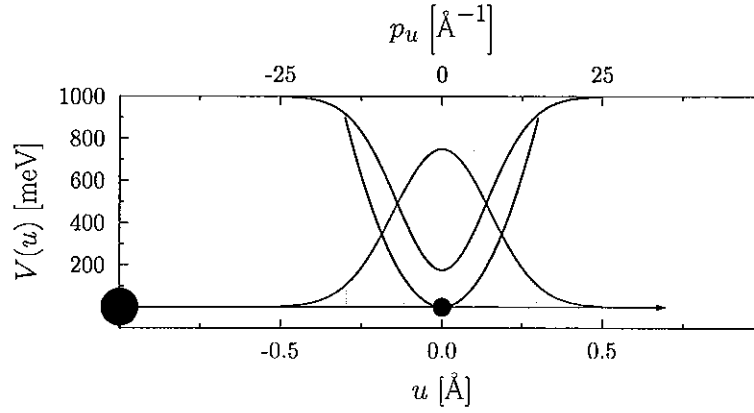


Fig. 3. – A pictorial representation of the square-modulus of the wave function, and its associated NMD along a generic axis  $u$  of a covalent bond between two atoms.

This physical quantity is the diagonal matrix element in the  $p$ -representation of the single-nucleus reduced density matrix, with  $\Psi(\mathbf{x})$  being the spatial wave function, that is, the solution of the Schrodinger equation for a given potential  $V(\mathbf{x})$ . In the same way as the function  $|\Psi(\mathbf{x})|d\mathbf{x}$  quantifies the probability to find a particle in the small volume between  $\mathbf{x}$  and  $\mathbf{x} + d\mathbf{x}$ ,  $n(\mathbf{p})d\mathbf{p}$  describes the probability for the nucleus to have a momentum vector between  $\mathbf{p}$  and  $\mathbf{p} + d\mathbf{p}$ . Therefore, the unit-sum rule applies, that is

$$(15) \quad \int_{-\infty}^{\infty} n(\mathbf{p})d\mathbf{p} = \int_{-\infty}^{\infty} |\Psi(\mathbf{x})| d\mathbf{x} = 1.$$

Because of the wave-like character of the nuclei as quantum particles, and the relation through a Fourier transform of the two canonical variables  $\mathbf{p}$  and  $\mathbf{x}$ , the Heisenberg uncertainty principle holds for any component  $u$  of the position vector  $\mathbf{x}$ , that is

$$(16) \quad \Delta u^2 \Delta p_u^2 \sim \frac{\hbar^2}{4}.$$

A pictorial representation of the relation between the wave function, the NMD, and the underlying local potential affecting the nucleus is shown in fig. 3 for a one-dimensional potential, and in fig. 4 for isotropic and anisotropic two-dimensional potentials. In particular, the left-hand side of fig. 4 shows the two-dimensional harmonic potentials at the centre of which a nucleus has its average position. The deformation of the multivariate potential in fig. 4 can be interpreted as arising from the presence of a chemical bond —i.e., the OH bond in water. In such case, the motion of the proton would be hindered along the  $y$ -direction in the figure, while the mean-square displacement in the perpendicular direction,  $x$ , could be larger because the potential (that in the case of the water could arise from intermolecular hydrogen bonding) would be less steep. The central part of fig. 4 shows the square of the wave function of the nucleus solving the Schrodinger equation for both isotropic and anisotropic cases. The wave function is shaped according to the potential, being shorter along the covalent-bond axis and broader in the other direction. It is important to note how a rotational average of the multivariate squared

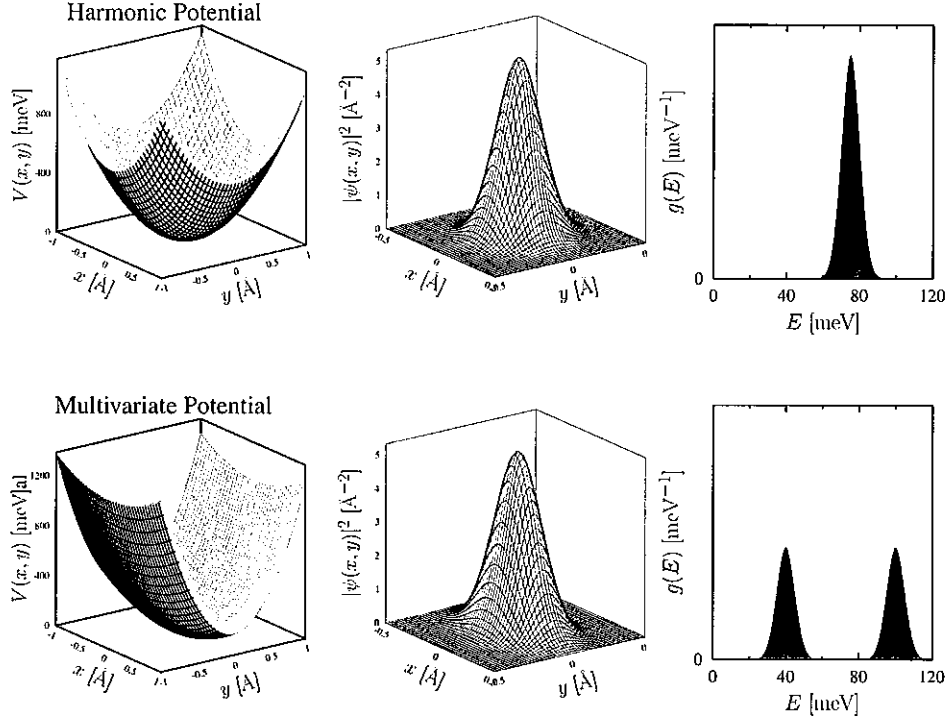


Fig. 4. – The link between the local potential affecting a nucleus (left), the square of the nuclear wave function (centre), and the corresponding density of vibrational states (right) in the case of a harmonic and isotropic potential (top) and a harmonic and anisotropic potential (bottom).

wave function (or NMD) does not correspond to a univariate function. Finally, the right part of fig. 4 sets the scene for a subsequent discussion in sect. 2'4 on the link between the NMD and the wave function, and the vibrational density of states of the system, therefore linking the single-particle dynamics of the nucleus to the dynamics of the entire many-body system.

As hinted above, the NMD of the struck particle broadens the scattering response by a mechanism similar to the Doppler broadening of spectral lines in atomic and molecular spectroscopy. Despite this broadening, the signal from recoil lines of different elements are, in principle, separable, making it possible to perform simultaneous measurements of the NMDs of H, D and O in water. Within the IA, the two dynamic variables,  $\hbar\omega$  and  $\hbar Q$ , can be related via the definition of the West-scaling variable  $y$  [119,120]

$$(17) \quad y = \vec{p} \cdot \hbar \hat{Q} = \frac{M}{\hbar^2 Q} (\hbar\omega - \hbar\omega_r).$$

The recoil peak defines a parabolic trajectory in  $(Q, \omega)$  space. Since the position in  $(Q, \omega)$  space depends on the mass,  $M$ , of the recoiling particle, particles of different mass can be distinguished in the measured spectrum.

The incoherent dynamic structure factor in the IA, eq. (13), can then be rewritten in

the form

$$(18) \quad S_{IA}(\mathbf{Q}, \omega) = \frac{M}{\hbar Q} J_{IA}(y, \hat{\mathbf{Q}}),$$

where  $J_{IA}(y, \hat{\mathbf{Q}})$  is the Neutron Compton Profile (NCP) defined as

$$(19) \quad J_{IA}(y, \hat{\mathbf{Q}}) = \hbar \int \mathbf{n}(\mathbf{p}') \delta(\hbar y - \mathbf{p}' \cdot \hat{\mathbf{Q}}) d\mathbf{p}'.$$

The quantity  $\hat{\mathbf{Q}}$  is a unit vector, as  $J_{IA}(y, \hat{\mathbf{Q}})$  no longer depends on the magnitude of  $\mathbf{Q}$ . Physically,  $J_{IA}(y, \hat{\mathbf{Q}})dy$  corresponds to the probability for a nucleus to have a momentum parallel to  $\hat{\mathbf{Q}}$  of a magnitude between  $\hbar y$  and  $\hbar(y + dy)$ . In an isotropic system, the direction  $\hat{\mathbf{Q}}$  is no longer relevant, and eq. (19) can be re-written as

$$(20) \quad J_{IA}(y) = 2\pi\hbar \int_{|\hbar y|}^{\infty} p n(p) dp.$$

$n(\mathbf{p})$  can then be reconstructed from  $J_{IA}(y, \hat{\mathbf{Q}})$  from eq. (20) yielding

$$(21) \quad n(p) = -\frac{1}{2\pi\hbar^3 y} \frac{d}{dy} J_{IA}(y)|_{\hbar y=p}.$$

The single-particle mean kinetic energy,  $\langle E_K \rangle$ , is related to the second moment of  $J_{IA}(y)$  via

$$(22) \quad \langle E_K \rangle = \frac{3\hbar^2}{2M} \int_{-\infty}^{\infty} y^2 J_{IA}(y) dy = \frac{3\hbar^2}{2M} \sigma_y^2,$$

where  $\sigma_y$  is the standard deviation of the NCP.

**2.2. Validity of the impulse approximation and corrections at finite  $Q$ .** – The IA is strictly valid only in the asymptotic double limit  $(Q, \hbar\omega) \rightarrow \infty$ , keeping  $y$  constant. For finite values of the energy and wave vector transfers, the longitudinal momentum distribution retains an additional dependence on  $Q$  which is known as Final State Effects (FSE). The modeling of FSEs has been a much discussed topic in the early days of DINS [121-131]

The first point to stress regarding the validity of the IA is that the scattering is incoherent, *i.e.*, that the energy of the incident particle is much larger than the binding energy of the target particle, see *e.g.* [132]. This applies when atomic nearest-neighbour distances are much greater than  $2\pi/Q$ , so that the interference of the scattering amplitudes from different particles averages to zero.

In 1984, Gunn and Warner showed that, by treating model systems of harmonically bound particles, an asymptotic analysis under conditions of high  $Q$  results in a particle looking as though it were unbound. In other words, the weighting (envelope) of the various inelastic channels is that of a free particle, although the discreteness of the allowed energy transfers reflects the fact that the particles are, in reality, bound [133]. The resultant incoherent scattering from a particle in the lattice resembles that from a

free particle (Gaussian centred at the recoil energy) but with a width determined by the lattice density of states and the temperature.

Historically, it was the seminal work by Gunn *et al.* [40], that showed that the key is in the natural interpretation of large momentum transfers yielding apparent scattering from a free particle. They first made the relation between the classical notions of impulsive forces and the WKB approximation, as applied to the derivation of the neutron scattering law connection to the nuclear momentum distribution. Particularly, the authors noted that the target particle, in its final state, looks like a free particle (*i.e.* highly excited states are plane waves), at least in the region where the ground-state wave function is significant [40]. This assumption has one critical consequence in the context of the applicability of the DINS method to condensed matter studies and also reconciles the apparent free-particle final state with scattering from particles in unbounded and steep potentials. These are, for example, particle undergoing Brownian motion [134], or a particle in a hard sphere gas [135, 136], which are never “free” even on the shortest time scales. Real systems will always have finite forces acting on the target particle and will approach the IA limit at sufficiently large  $Q$ . Namely, it allows for a wide class of local, effective Born-Oppenheimer potentials, felt by nuclei, to be used to model NMDs that are sampled by epithermal neutrons. Mathematically, the class of allowed potentials, bring in the second ingredient implicit in the validity of the IA, *i.e.* the short-time approximation embodied in eq. (8). These potentials can be written as

$$(23) \quad V(x) = V_0(x/a)^{2r},$$

which in the limit  $r \rightarrow \infty$  yields an infinite square well of width  $2a$ . The notion that the interaction time,  $\tau$ , is associated with the scattering process was introduced by Gunn *et al.* [40]. It is expressed in term of the single-particle correlation function introduced in eq. (10) and represents the decay time of the correlation function  $Y_{jj}(\mathbf{Q}, t)$ . This decay time is due to phase mixing (see eq. (12)) as a consequence of the spread in velocities of the particles [114, 122, 137, 138]. The interaction time is valid under the assumption that, the spatial spread of the wavepacket is much smaller than the spatial extent of the wave function of the target particle in the ground state,  $l$ . Under this assumption,  $\tau$  can be written as

$$(24) \quad \tau = \frac{2ml}{2p_n + \hbar Q}.$$

As shown above, the interaction time is related to the inverse of the average of the neutron initial and final mean velocities [114, 122, 137, 138]. Then the IA holds in the presence of no significant deviations from a free-particle motion over a time  $\tau$ . This will be the case for hydrogenous systems where scattering occurs from a localized particle and then  $\tau$  falls in the attosecond time scale.

In the following, we determine when the IA is valid and what the corrections are, bearing in mind that the experiments are typically done far into the limit where this approximation is valid.

We recall that for finite values of the energy and wave vector transfers, the longitudinal NMD retains an additional dependence on  $Q$  known as FSEs [121]. FSEs are due to the localization of the struck atom in its final state by surrounding atoms. These make the momentum of the final state uncertain and since the dynamic structure factor, in eq. (13), is determined by the Fourier transform of the product of initial and final state

wave functions, the momentum in the initial state is also uncertain. This introduces a broadening of the observed  $J(y)$ , similar to an instrumental resolution broadening. Historically, Hohenberg and Platzman [108] were the first to include deviations from free-particle motions in the final state. They showed that these deviations produce a Lorentzian broadening into the dynamical structure factor proportional to  $Q$ . Further studies [122, 123, 125] demonstrated that the NMD plays also an important role in the broadening. Subsequently, other authors [126-129] have provided slightly different expressions for the broadening. A general feature resulting from these studies is that in the presence of FSEs the NCP becomes  $Q$ -dependent. This follows the original framework proposed by Sears [139], who accounted for these deviations by adding corrections to first order in  $1/Q$ : the IA is the first term in the  $1/Q$  expansion of  $S(\mathbf{Q}, \omega)$  and corresponds to the physical situation where the struck atom is imparted such a high momentum, that it can be considered as recoiling freely. The correction for finite  $Q$  is due to the effect of the forces on the particle producing displacements from straight-line trajectories on the timescale  $\tau$  defined earlier [31]. Thus the  $J(y, \hat{Q})$  needs to be replaced by  $J(y, \mathbf{Q})$ , and its relationship with the  $S_{\text{IA}}(\mathbf{Q}, \omega)$  in eq. (18) yields the following expression:

$$(25) \quad J(y, \mathbf{Q}) = \frac{\hbar Q}{M} S(\mathbf{Q}, \omega).$$

For the isotropic case, the effect of these deviations on  $J(y, \mathbf{Q})$  is described as a series in powers of  $1/Q$  [138]

$$(26) \quad J(y, Q) = \left[ 1 - \frac{A_3}{Q} \frac{d^3}{dy^3} J_{\text{IA}}(y) + \frac{A_4}{Q^2} \frac{d^4}{dy^4} J_{\text{IA}}(y) + \dots \right],$$

where it can be shown that  $A_3$  and  $A_4$  are simply related to the inter-particle potential  $V$  via

$$(27) \quad A_3 = \frac{M}{36\hbar^2} \langle \nabla^2 V \rangle; \quad A_4 = \frac{M^2}{72\hbar^4} \left\langle \left( \vec{\nabla} V \right)^2 \right\rangle,$$

where the symbol  $\langle \dots \rangle$  stands for a quantum-statistical average. The extension to the case of anisotropic NMDs is given in ref. [140].

For finite  $Q$ , and up to the first order of  $Q$ , eq. (26) yields

$$(28) \quad J(y, Q) = \left( 1 - A_3(Q) \frac{\partial^3}{\partial y^3} \right) J(y) = J_{\text{IA}}(y) + \Delta J_{\text{IA}}(y, Q).$$

In the assumption of a mainly Gaussian NCP, the correction for FSEs,  $\Delta J(y, Q)$  can be expressed analytically as

$$(29) \quad \Delta J(y, Q) = -A_3(Q) \frac{\partial^3}{\partial y^3} J_{\text{IA}}(y) = \frac{A_3(Q)}{\sigma^3 2^{3/2}} H_3 \left( \frac{y}{\sqrt{2}\sigma} \right) J_{\text{IA}}(y).$$

Moreover, for an isotropic harmonic potential, one has

$$(30) \quad A_3(Q) = \frac{M^2 \omega^2}{12\hbar^2 Q} = \frac{\sigma^4}{3Q},$$

and consequently

$$(31) \quad \Delta J(y, Q) = \frac{\sqrt{2}\sigma}{12Q} H_3 \left( \frac{y}{\sqrt{2}\sigma} \right) J_{IA}(y).$$

However, it is often necessary during the data analysis to relax the Gaussian approximation, and replace the  $Q$ -independent factor with a free parameter  $C_\Delta$ , so as to have

$$(32) \quad \Delta J(y, Q) = \frac{C_\Delta}{Q} H_3 \left( \frac{y}{\sqrt{2}\sigma} \right) J_{IA}(y).$$

If one considers the NCP expressed by eq. (44), by applying the third derivative to the terms up to  $n = 3$  in the series, one has

$$(33) \quad J(y, Q) = J_{IA}(y) \sum_{n=0,2,3} C_{2n} \left[ H_{2n} \left( \frac{y}{\sqrt{2}\sigma} \right) + \frac{C_\Delta}{Q} H_{2n+3} \left( \frac{y}{\sqrt{2}\sigma} \right) \right].$$

A final comment regards the contribution of FSEs to experimental DINS data obtained on the VESUVIO spectrometer. In this instrument, the  $Q$  varies over the range  $20 \text{ \AA}^{-1} < Q < 250 \text{ \AA}^{-1}$ , thus FSE are strongly suppressed.

**2'3. Extracting momentum distributions and mean kinetic energies.** – The NMD, the ultimate observable of a DINS experiment, appears as a spectral broadening along a mass-specific recoil line, that can be related to the underlying potential-energy landscape in a model-free fashion [111,141,142]. However, for the purpose of the analysis of experimental data, it is often necessary to provide an analytic description of the NCP [93,143]. There are two primary methods currently used to express NCPs and NMDs in the most general way. The first one, proposed by Reiter and Silver [114], suggested the use of orthonormal bases of the Hilbert space [31]. In particular the NCP is expressed as a Gauss-Hermite (or Gram-Charlier) polynomial expansion of the form

$$(34) \quad J_{IA}(y) = \frac{1}{\sqrt{2\pi}\sigma} \exp \left[ -\frac{y^2}{2\sigma^2} \right] \sum_{n=0}^{\infty} \frac{c_{2n}}{2^{2n}n!} H_{2n} \left( \frac{y}{\sqrt{2}\sigma} \right).$$

where  $H_{2n}$  are Hermite polynomials and  $c_{2n}$  the corresponding coefficients. This function is linked to the NMD by a Radon transformation [31,114]. The NMD, expressed in terms of a Gaussian times a series of Laguerre polynomials  $L_n^{\frac{1}{2}}(\frac{p^2}{2\sigma^2})$  with coefficients  $(-1)^n a_n$ , yields

$$(35) \quad n(p) = (2\pi\sigma^2)^{-\frac{3}{2}} \exp \left[ -\frac{p^2}{2\sigma^2} \right] \sum_n (-1)^n a_n L_n^{\frac{1}{2}} \left( \frac{p^2}{2\sigma^2} \right).$$

In the expressions above,  $\{a_n\} = \{c_{2n}\}$  are set of coefficients for which the conditions  $a_0 = c_0 = 1$  and  $a_1 = c_2 = 0$  are required. The former condition allows for the unit-sum rule to be satisfied, while the latter allows the interpretation of  $\sigma^2$  as the second moment of  $J_{IA}(y)$  independently of the value of any other coefficient  $a_n$  with  $n > 1$ ,

$$(36) \quad \int_{-\infty}^{\infty} y^2 J_{IA}(y) dy = \sigma^2.$$

In this sense,  $\sigma^2$  can be interpreted as the mean-square momentum of the nucleus, and can be related to its mean kinetic energy  $\langle E_K \rangle$  accordingly to the classical dispersion relation

$$(37) \quad \langle E_K \rangle = \frac{\hbar^2 \sigma^2}{2M}.$$

In the case of a crystal, in order to obtain the NMD, one performs the inversion of  $J(y, \hat{\mathbf{Q}})$  (see eq. (19)) [114]. This inversion is easily accomplished for the cases where  $J(y, \hat{\mathbf{Q}})$  is independent of orientation, as in a powder measurement or a fluid (see eq. (21)). Because of the increasing factor  $2^{2n} n!$ , higher-order polynomials can be fitted (see sect. 2'6.2) only in rare cases [98]; in particular  $c_6$  is the highest coefficient derived so far in several recent studies [94-97, 99, 101, 110, 146]. Moreover, one should also notice that the NCP when all coefficients  $n > 0$  vanish, that is a simple Gaussian function, corresponds to the solution of a harmonic and isotropic local potential. Although eq. (34) has the most general form, the weakness of this parametric model is the difficult physical interpretation of the coefficients multiplying the Hermite polynomials and often to separate the effects of anharmonicity from those of anisotropy is far from being trivial [93].

In the second parametric model, corresponding to the case of a harmonic and anisotropic local potential, the NMD is expressed using a three-dimensional multivariate anisotropic Gaussian lineshape,  $J(y, \hat{\mathbf{Q}})$ , [11, 16, 92, 93, 110, 143, 144]. For polycrystalline samples it is reasonable and at the same time insightful to assume that the underlying  $n(p)$  arises from the spherical average of an anisotropic multivariate Gaussian distribution, with three distinct frequencies  $\omega_{x,y,z}$  associated with local and orientation-dependent principal axes of the molecule. This approach corresponds to an anisotropic quasi-harmonic model in which the main effects of anharmonicity are accounted for by the effective frequencies  $\omega_i$  [93]. In other words, the NMD can be expressed as

$$(38) \quad n(p) = \left\langle \frac{1}{\sqrt{8\pi^3 \sigma_z \sigma_x \sigma_y}} \exp \left( -\frac{p_z^2}{2\sigma_z^2} - \frac{p_x^2}{2\sigma_x^2} - \frac{p_y^2}{2\sigma_y^2} \right) \right\rangle_{\Omega},$$

where  $\langle \dots \rangle_{\Omega}$  denotes the angular average of the three-dimensional NMD,  $n(\mathbf{p})$ , over all the possible orientations of the molecule in the reference of frame of the laboratory. This expression involves three parameters —the variances  $\sigma_{i=x,y,z}^2$  being related to the principal frequencies by  $\sigma_i^2 = \frac{M\omega_i}{2\hbar} \coth \frac{\beta\hbar\omega_i}{2}$  or to the three components of the quantum kinetic energy by  $\langle E_K \rangle = 3\hbar^2 \sigma^2 / 2M$ . This parametric model introduced above (eq. (38)) provides a suitable framework to assess the main effects of anharmonicity via a determination of the characteristic frequencies  $\omega_i$ .

The expression of the NCP for a multivariate Gaussian becomes

$$(39) \quad J_{1A}(y) = \frac{1}{\sqrt{2\pi\sigma_x\sigma_y\sigma_z}} \int_{\Omega} \frac{d\Omega}{4\pi} \exp \left[ -\frac{y^2}{2S^2(\theta, \phi)} \right] S^2(\theta, \phi),$$

where the angular-dependent standard deviation in the anisotropic system is defined as

$$(40) \quad \frac{1}{S^2(\theta, \phi)} = \sin^2 \theta \left( \frac{\cos^2 \phi}{\sigma_x^2} + \frac{\sin^2 \phi}{\sigma_y^2} \right) + \frac{\cos^2 \theta}{\sigma_z^2}.$$

OK?

In this case, eq. (36) for the second moment of the NCP becomes

$$(41) \quad \int_{-\infty}^{\infty} y^2 J_{IA}(y) dy = \frac{\sigma_x^2 + \sigma_y^2 + \sigma_z^2}{3} = \bar{\sigma}^2.$$

2'4. *Nuclear momentum distributions in the harmonic approximation.* – Due to the general form of eq. (34), one can express the NCP arising from the harmonic and anisotropic potential as a sum of elements of the Gauss-Hermite basis [145]. In particular, by imposing that the second, fourth, and sixth moments of the NCP have to be the same when evaluated from eqs. (34) and (39), one finds the conditions [146]

$$(42) \quad C_4 = c_4(\sigma_x, \sigma_y, \sigma_z) = \frac{2}{15} \left( \frac{\sigma_x^4 + \sigma_y^4 + \sigma_z^4}{\sigma^4} - 3 \right)$$

and

$$(43) \quad C_6 = c_6(\sigma_x, \sigma_y, \sigma_z) = \frac{8}{315} \left( \frac{\sigma_x^6 + \sigma_y^6 + \sigma_z^6 + 6\sigma_x^2\sigma_y^2\sigma_z^2}{\sigma^6} - 9 \right),$$

that can be used, together with the definition of  $\bar{\sigma}^2$  in eq. (41), to express the multivariate NCP as Gauss-Hermite expansion up to  $n = 3$  as

$$(44) \quad J_{IA}(y) = \frac{1}{\sqrt{2\pi\bar{\sigma}}} \exp \left[ -\frac{y^2}{2\bar{\sigma}^2} \right] \left[ 1 + C_4 H_4 \left( \frac{y}{\sqrt{2\bar{\sigma}}} \right) + C_6 H_6 \left( \frac{y}{\sqrt{2\bar{\sigma}}} \right) \right].$$

This model could be improved by imposing similar conditions for higher moments of the NCP, yet the differences between a fine-grid numerical integration of eq. (39) and the analytic expression using eq. (34) are much lower than experimental error bars in DINS spectra [145]. Moreover, when the angular integration in eq. (39) is performed numerically, the analysis of the experimental data suffers from time-consuming calculations and numerical errors from the finite size of the integration grid used to map the variables  $\theta$  and  $\phi$  [144, 145]. Interestingly, the possibility to express a multivariate NCP as a sum of Gauss-Hermite polynomials highlights the difficulty in the interpretation of the coefficient  $c_{2n}$  in the most general case. In particular, eq. (34) does not allow to discriminate between the effects of anharmonicity along a given direction or to highlight the presence of an underlying anisotropy [114, 140]. In contrast, the second approach from eqs. (39) and (44) provides a suitable framework to assess the main effects of anharmonicity via a determination of the parameters  $\{\sigma_i\}$ .

2'5. *The physical origin of nuclear momentum distributions.* – In very general terms [147], the dynamics of a system composed of interacting particles can be expressed by a Hamiltonian that is a function of the momentum  $\mathbf{p}_i$  and the position  $\mathbf{x}_i$  of every particle  $i$ , that is

$$(45) \quad H(\mathbf{x}, \mathbf{p}) = \sum_i \frac{\mathbf{p}_i^2}{2M_i} + \sum_{i,j} V(\mathbf{x}_i, \mathbf{x}_j),$$



where the sole assumption is that only two-body interactions between atoms  $i$  and  $j$  are considered. When a statistically significant ensemble of particles is considered, such as the ensemble of atoms in a macroscopic sample, the average values of the above quantities can be considered, and one has

$$(46) \quad \langle H \rangle = \sum_i \langle E_K \rangle_i + \langle V \rangle,$$

with  $\langle H \rangle$  and  $\langle V \rangle$  representing the mean values of the total and potential energies, respectively. The interaction potential  $V$  can adopt one of the many common forms in condensed-matter physics and chemistry, as the London, van der Waals, or Morse potentials. However, the harmonic potential is often a suitable starting point. In the case of spring-like forces defined by the parameters  $f_{ij}$ , the simpler formulation

$$(47) \quad H(\mathbf{x}, \mathbf{p}) = \sum_i \frac{\mathbf{p}_i^2}{2M_i} + \sum_{i,j} \frac{1}{2} f_{ij} (\mathbf{x}_i - \mathbf{x}_j)^2$$

can be tackled mathematically and one can look for analytic solutions. In particular, in the framework of quantum mechanics, and based on the procedure of second quantisation, it is useful to replace the canonical variables  $\{\mathbf{x}_i, \mathbf{p}_i\}$  with a set of harmonic oscillators of frequency  $\{\omega_k\}$  that can be created and destroyed by Dirac operators  $b_k$  and  $b_k^\dagger$ . After a thorough diagonalisation of the basis, the Hamiltonian of the system reduces to the form

$$(48) \quad H = \sum_k \hbar \omega_k \left( b_k^\dagger b_k + \frac{1}{2} \right) = \hbar \omega_k \left( n_k + \frac{1}{2} \right),$$

where  $n_k = b_k^\dagger b_k$  defines the number of harmonic oscillators of frequency  $\omega_k$  that have been created in the system. Due to the quadratic form with which both momentum and position enter eq. (47), and the symmetry in their roles when the Hamiltonian is expressed in the new basis of harmonic oscillators, the mean value of the total energy of the system is shared in equal amounts by the kinetic and potential terms, and eq. (48) can be expressed as

$$(49) \quad \frac{\langle H \rangle}{2} = \sum_i \langle E_K \rangle_i = \langle V \rangle = \sum_n \langle n_k \rangle \frac{\hbar \omega_k}{4}.$$

Notably, the average kinetic energy is equal to half of the total energy only within the harmonic approximation. To illustrate the above, two cases involving anharmonic oscillator can be considered, namely symmetric and antisymmetric [148]. In the first case, described by a potential of the form  $V_S(x) = 1/2 k x^2 - 1/4 b x^4$ , to second order in the anharmonicity parameter,  $\delta = b A^2/k$  with  $A$  being the amplitude of the unperturbed harmonic motion, one has

$$(50) \quad \frac{\langle E_K \rangle}{\langle H \rangle} = \frac{1 - 12\delta/16}{2(1 - 9\delta/16)}.$$

Equation (50), in the limit of large anharmonicity of, say,  $\delta = 0.1$ , yields the average kinetic energy being 0.49 of the total energy, thus rendering the anharmonic correction very

small for this class of potentials. Moreover, in the asymmetric case, described by a potential of the form  $V_A(x) = 1/2kx^2 - 1/3ax^3$ , to first order in the anharmonic parameter,  $\delta = Aa/k$ , the result is the same as in the case of purely harmonic oscillator [148].

Equation (49) represents a remarkable link between the vibrations in the system and the mean kinetic energy of a nucleus. Apart from the harmonic assumption, eq. (49) holds some generality in the way it can be applied. The vibrations represented by  $\omega_k$  can refer to the lattice and phonon modes of a crystal, as well as to the normal modes of vibrations for an isolated molecule. The latter case will be referred to abundantly in the next section, as it allows for an insightful interpretation of the dynamics of the water molecule in a variety of systems. Moreover, one can overcome the isolated-molecule picture by replacing the frequency of the ideal normal modes with experimentally measured frequencies that include, in a phenomenological fashion, the effect of the interactions amongst neighbour molecules.

However, the higher the complexity of a system, for example because of the lack of long-range order in liquids and amorphous solids, the more convenient is to consider a vibrational density of states (VDoS),  $G(\omega)$ . The contribution of the vibrations to the motion of each atom of mass  $M$  is expressed by means of the atom-projected VDoS,  $G_M(\omega)$ , a function that takes into account, for every vibration, the dispersion relation and the projection of the probe momentum transfer  $\mathbf{Q}$  onto the polarisation vector [31, 149, 150]. As  $G(\omega) = \sum_M G_M(\omega)$ , eq. (49) can be now expressed as [68, 151]

$$(51) \quad \langle E_K \rangle_M = 3 \int_0^\infty \frac{\hbar\omega}{4} \langle n(\omega) \rangle G_M(\omega) d\omega,$$

where for a “directionally averaged”  $G(\omega)$  a factor 3 needs to be introduced. As the integral is weighted by the frequency  $\omega$ , one should expect high-energy modes to contribute the most to the total kinetic energy of a nucleus, especially in the case of hydrogen. Because of the Bose-Einstein statistics applied to vibrations, the expectation value of the number operator can be expressed according to

$$(52) \quad \langle n(\omega) \rangle = \coth \left( \frac{\hbar\omega}{2k_B T} \right),$$

that is, whenever the energy of the vibration is much higher than the thermal contribution  $k_B T$ ,  $\langle n(\omega) \rangle \simeq 1$  and eq. (51) is consequently simplified. In the case when this condition is satisfied for each vibrational frequency, the value of the mean kinetic energy corresponds to the case of a thermodynamic temperature near absolute zero, and the dynamics of the system is completely defined by ZPEs.

The mean kinetic energy of a nucleus, already defined in previous sections based on the formalism of the NMD, is linked to the formalism of this section by

$$(53) \quad \langle E_K \rangle_M = \left\langle \frac{\mathbf{p}_i^2}{2M_i} \right\rangle = \frac{\langle \mathbf{p}_i^2 \rangle}{2M} = \frac{\hbar^2 \sigma_M^2}{2M},$$

where  $\langle \dots \rangle$  is to be understood as the average over the ensemble of particles of mass  $M$ . This definition is dictated by the experimental ability of DINS to resolve the contributions from atoms of different masses. However, atoms of the same isotope subjected to different chemical environments need to be included in the same statistical ensemble average. In the case of water, this means that the proton mean kinetic energy could correspond to

the average over hydrogen atoms experiencing different degrees of hydrogen bonding. We can also relate the root-mean-square value of the atom's momentum,  $\langle \mathbf{p}_i^2 \rangle$ , to the width of the NMD,  $\sigma^2$ . The width of the NMD in the isotropic and harmonic case is therefore related to  $\langle E_K \rangle_M$  by

$$(54) \quad n(p) = \left[ \frac{4}{3} \pi M \langle E_K \rangle_M \right]^{-3/2} \exp \left[ -\frac{3p^2}{4M \langle E_K \rangle_M} \right].$$

Equation (54) has the same analytic form as for the classical result of a gas of weakly interacting particles. In the case of an ideal gas, the value of the mean kinetic energy predicted in the MB theory [152] is

$$(55) \quad \langle E_K \rangle_{MB} = \frac{3}{2} k_B T.$$

Thus, one can define an effective temperature for each atom in the system defined as [153]

$$(56) \quad T_M^* = \frac{2}{3} \langle E_K \rangle_M.$$

This effective temperature has a more profound interpretation than global parameters of a system of interacting atoms, such as the Debye temperature, as it is atom-specific, and weights atom-projected motions according to the local dynamics of every atom. This approach suggests that NQEs could be incorporated into a simulation by artificially raising the temperature of each atom [154]. The same concept can be recognised as one of the physical motivations behind the recent development of coloured-noise approaches in molecular-dynamics simulations [12]. Moreover, it is possible to define a Quantum-energy Excess (QE) of an atom's mean kinetic energy in a condensed-matter system as opposed to the case of an ideal gas, namely [100]

$$(57) \quad QE = \frac{\langle E_K \rangle_M}{\langle E_K \rangle_{MB}} = \frac{T_M^*}{T} = \frac{\hbar^2}{M k_B T} \sigma_M^2.$$

An example of the effect of QE on the dynamics of D and O in heavy water at 330 K is shown in fig. 5.

Finally, we can conclude this section by obtaining a formula for the prediction of the width of an NMD within the harmonic approximation. By combining eqs. (51) and (53), one finds

$$(58) \quad \sigma_M^2 = \frac{M}{2} \int_0^\infty \frac{\hbar \omega}{2} G_M(\omega) \coth \left( \frac{\hbar \omega}{2 k_B T} \right) d\omega.$$

The power of eq. (58) lies on its applicability to joint studies of Inelastic Neutron Scattering (INS) and DINS. As noted, DINS probes the ground state of a nucleus in its local potential, as opposed to INS probing the jump from the ground state to an excited state associated with the creation of a vibrational mode. In this sense, deviations of the measured width of a momentum distribution from the prediction associated to eq. (58) can highlight the deviation from the assumed harmonicity of the potential. The case is pictorially shown in fig. 6, where DINS and INS measurements on amorphous ices, discussed

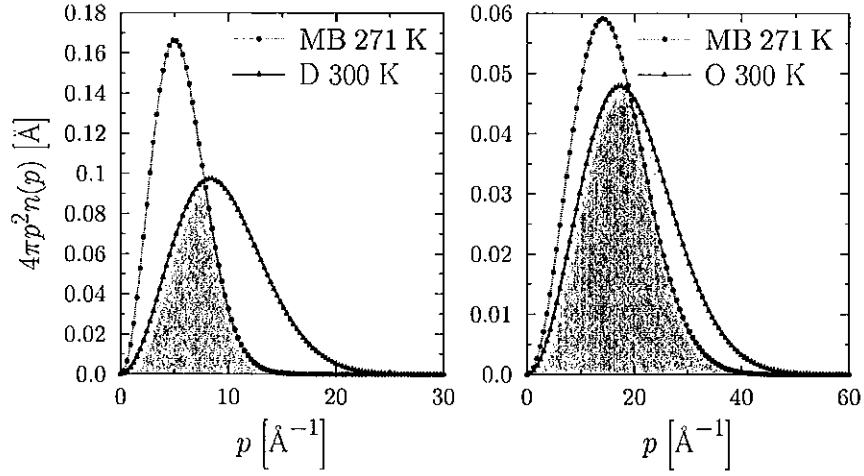


Fig. 5. – The radial NMDs for D (left) and O (right) in  $D_2O$  at 300 K taken from ref. [12]. This example has been chosen to illustrate the drastic difference between an MB prediction and the experimental results.

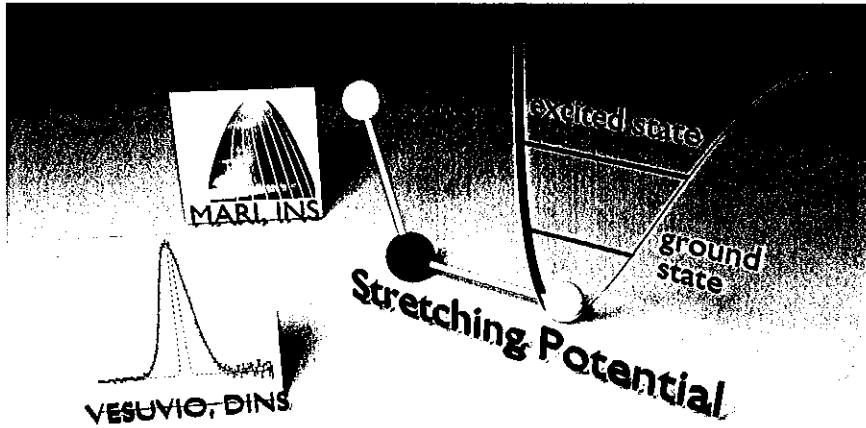


Fig. 6. – Pictorial description of the comparison of INS and DINS data that can underline the anharmonicity of the local potential affecting hydrogen in the water molecule. The experimental data refer to the case of amorphous ices from ref. [94]. The DINS and INS measurements have been performed on the VESUVIO and MARI spectrometer, respectively.

in a later section, allow for the reconstruction of the shape of the potential affecting the hydrogen dynamics in the water molecule. The comparison between the experimental results from the two techniques is enabled, within the incoherent approximation, by assuming that a INS spectrum of a system containing hydrogen is dominated by the signal from the neutron scattering from the proton. The same equation can be applied to a calculated atom-projected VDoS, *e.g.* in phonon calculations using Density Functional Theory (DFT) perturbation theory where the dynamical matrix is solved directly for a

given reciprocal lattice vector  $\mathbf{Q}$  [155]. Full illustration of the formalism for crystalline materials can be found in ref. [33]. However, one should notice that state-of-the-art simulations of liquids and disordered materials are based on the exact evaluation of the NMD,  $n(p)$ , from the density matrix,  $\rho(\mathbf{r}, \mathbf{r}')$ , namely [12, 18, 156, 157]

$$(59) \quad n(\mathbf{p}) = \frac{1}{(2\pi\hbar)^3} \int d\mathbf{r} d\mathbf{r}' \exp \left[ \frac{i}{\hbar} \mathbf{p} \cdot (\mathbf{r} - \mathbf{r}') \right] \frac{\rho(\mathbf{r}, \mathbf{r}')}{Z},$$

where  $Z = \int d\mathbf{r} \rho(\mathbf{r}, \mathbf{r})$  is the partition function, and

$$(60) \quad \rho(\mathbf{r}, \mathbf{r}') = \langle \mathbf{r} | \exp \left( -\frac{H}{k_B T} \right) | \mathbf{r}' \rangle.$$

Additional details on the technicalities of PI simulations can be found in refs. [9, 158-160]. In the same framework, one can define the end-to-end spatial distribution as

$$(61) \quad n(\mathbf{x}) = \int d\mathbf{r} d\mathbf{r}' \rho(\mathbf{r}, \mathbf{r}') \delta(\mathbf{r} - \mathbf{r}' - \mathbf{x}) = \frac{1}{(2\pi\hbar)^3} \int d\mathbf{p} \exp \left( -\frac{1}{\hbar} \mathbf{p} \cdot \mathbf{x} \right) n(\mathbf{p}),$$

and is possible to express the neutron Compton profile as [18, 111]

$$(62) \quad J(y, \hat{\mathbf{Q}}) = \frac{1}{2\pi\hbar} \int dx_{\parallel} n(x_{\parallel}) \exp(-x_{\parallel} y),$$

where  $x_{\parallel} = \mathbf{x} \cdot \hat{\mathbf{Q}}$ , similarly to the previous definition of  $y = \mathbf{p} \cdot \hat{\mathbf{Q}}$ . Equation (60) is an application of Feynman mapping of the quantum system onto a set of replicas obeying classical mechanics, where each particle in a string of replicas is referred to as a “bead”, and adjacent beads interact via a harmonic potential of frequency  $\sim k_B T / \hbar$  [161]. In the case of an isotropic and harmonic potential, the mean force affecting a given atom in the system, after average over all interactions with neighbouring atoms, can be expressed in the simple form

$$(63) \quad f(x_{\parallel}) = \frac{M k_B^2 T^2}{\hbar^2} (QE - 1) x_{\parallel},$$

that is, the spring constants in eq. (47) show a non-trivial dependence upon thermodynamic and effective temperatures, and therefore on the QE. A detailed analysis of the mean force,  $f(x)$ , can be obtained by direct inspection of the experimental data in a model-independent way, as any deviations from linearity (typical of Hooke’s Law in eq. (63)) highlight the presence of anharmonicity.

## 2’6. Performing a DINS measurement

2’6.1. The measurement of neutron Compton profiles. In previous sections, the unique capabilities of DINS to probe NMDs and mean kinetic energies have been discussed. It has been mentioned that such Compton-like scattering is possible owing to the high values of the energy  $\hbar\omega$  and momentum  $Q$  transferred by the neutron to the scattering nucleus. In particular, to reach the IA one needs  $\hbar\omega \gg \hbar\omega_{\max}$ , where  $\omega_{\max}$  is the frequency of the highest-energy mode experienced by the scattering nucleus. As the highest vibrational

frequency in molecular spectroscopy is experienced by the proton in the  $\text{H}_2$  molecule at ca. 500 meV, the IA is reached when energy transfers in excess of several eV can be accessed experimentally. For this reason, DINS studies experienced a remarkable development with the advent of spallation neutron sources, epithermal neutrons not being readily available at research reactors.

Apart from rare cases [162, 163], accelerator-driven spallation sources produce neutrons in pulses, and the time-of-flight (ToF) technique [116, 117] is available in order to define the relation between the initial  $E_0$  and the final energy  $E_1$  of the neutron. The ToF technique is based on the measurement of the time  $t$  a neutron takes to “fly” the distance  $L_0$  from source to sample, and subsequently the distance  $L_1$  from sample to detector, namely

$$(64) \quad t - \tau = \sqrt{\frac{m}{2}} \left( \frac{L_0}{\sqrt{E_0}} + \frac{L_1}{\sqrt{E_1}} \right),$$

where  $\tau$  takes into account possible delays in the electronic chain of detection, and  $m$  is the mass of the neutron. If the final (initial) neutron energy is fixed through an energy analyser, ToF measurements can be used to obtain the initial (final) energy, and the energy transfer,

$$(65) \quad \hbar\omega = E_0 - E_1,$$

can be evaluated. Spectrometers fixing the final (initial) energy of the neutron are said to operate in the inverse-geometry (direct-geometry) mode. Moreover, by the knowledge of the position of the detector with respect to the sample investigated, defined by the angular coordinate  $\phi$  that  $L_1$  forms with  $L_0$ , the magnitude of the momentum transfer can be evaluated as

$$(66) \quad Q = \frac{\sqrt{2m}}{\hbar} \left( E_0 + E_1 - 2\sqrt{E_0 E_1} \cos \phi \right).$$

By combining this set of equations, it is possible to track the portion of the dynamic plane  $(Q, E)$  seen by each detector at scattering angle  $\phi$ . In particular, in the case of inverse-geometry spectrometers one can express the initial energy  $E_0$  as

$$(67) \quad E_0(E_1, Q, \phi) = E_1 \left( \cos \phi + \sqrt{\frac{\hbar^2 Q^2}{2mE_1} - \sin^2 \phi} \right) - E_1,$$

as opposed to the case of direct-geometry spectrometers, where one has an analogous expression for the final energy  $E_1$ , namely

$$(68) \quad E_1(E_0, Q, \phi) = E_0 - E_0 \left( \cos \phi \pm \sqrt{\frac{\hbar^2 Q^2}{2mE_0} - \sin^2 \phi} \right).$$

There are two key differences between direct and indirect spectrometers, as one can appreciate from eqs. (67) and (68), and from fig. 7. First, inverse-geometry spectrometers do not experience an upper bound for the energy and momentum transfers, as opposed

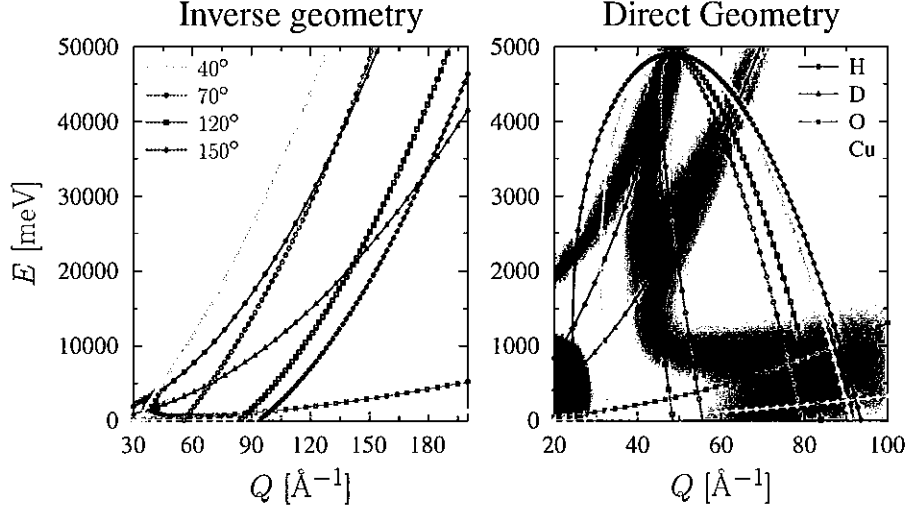


Fig. 7. – Calculated colour maps of the scattering intensity associated with atomic-recoil excitations for H, D, O, and Cu, as a function of energy and wave vector transfers using epithermal neutrons. The stationary atom-recoil excitations are reported as continuous black lines. Detector trajectories for scattering angles between 40 degrees and 150 degrees, for indirect- and direct-geometry configurations, are reported as orange-red markers, and correspond to  $E_1 = 4908$  meV and  $E_0 = 4908$  meV, respectively.

to the case of direct-geometry spectrometer. Moreover, inverse-geometry spectrometers cross each nuclear-recoil line only once and are almost tangent to the proton recoil line for forward-scattering detectors. On the other hand, eq. (68) provides two intersections of the recoil- and detector-trajectory lines for every scattering angle. References [32,33,164,165] provide an up-to-date appraisal of the complementarity between direct- and indirect-geometry spectrometers.

One of the major consequences of the IA, that the scattering intensity is concentrated along the mass-dependent recoil lines, makes of DINS a quite unique mass-resolved neutron-based technique. Spectra recorded by each detector show the NCP from each isotope in the system as virtually separated contributions. The mass selection capability is more effective for lighter elements, with the largest separation amongst isotopes for the case of H and D. Contrarily, as one approaches the infinite-mass limit, the scattering becomes almost elastic, and all recoil lines concentrate about the  $E = 0$  axis. Moreover, one should notice how the NCPs of light atoms from front-scattering detectors span a wide range of  $Q$ 's, as opposed to the case of heavy elements probed in backscattering detectors, where one can assume that  $Q$  is almost constant along a vertical line on the dynamical  $(Q, E)$  plane. More details on MAss-selective Neutron SpEctroscopy, often referred to as MANSE, can be found in [32,33,91,166-168].

In the light of the case studies discussed later, we focus now on the indirect-geometry spectrometer VESUVIO [36,37,61-63], at the ISIS pulsed neutron and muon source. In terms of energy and momentum transfers, VESUVIO provides routine access to  $0.5 \text{ eV} < \hbar\omega < 150 \text{ eV}$  and  $20 \text{ Å}^{-1} < \hbar Q < 300 \text{ Å}^{-1}$ , respectively. This wide coverage guarantees that the neutron scattering regime accessible in the experiments is well within the framework of the IA. A schematic layout of the instrument is reported in fig. 8.

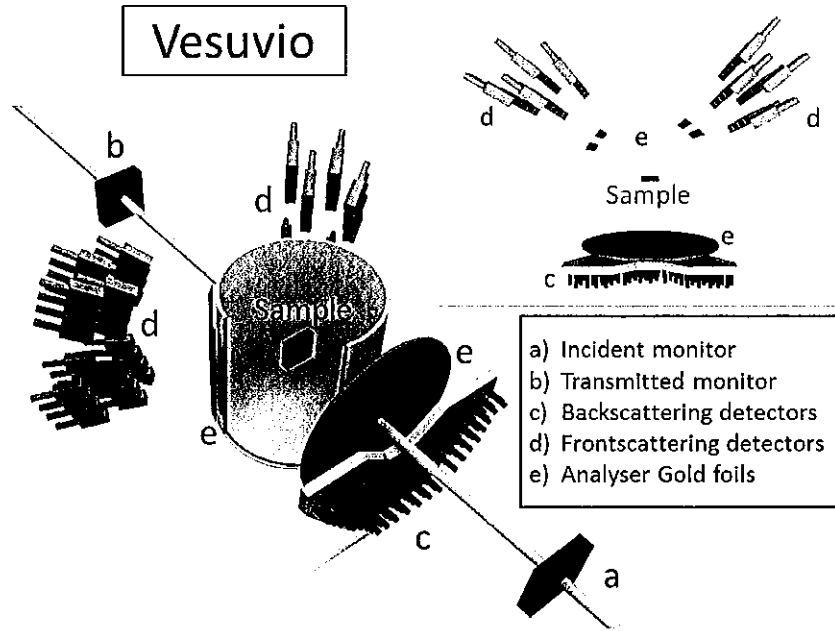


Fig. 8. – Schematic layout of the VESUVIO spectrometer: a) incident neutron monitor; b) transmission neutron monitor; c) Au resonance filters; d) forward scattering detectors; e) backward scattering detectors; s) sample.

By working in the indirect-geometry mode, the spectrum of incident neutrons  $I(E_0)$  available on VESUVIO is polychromatic and covers about 8 orders of magnitude, from a fraction of meV to hundreds of keV. VESUVIO views the room temperature water moderator of the ISIS Target Station 1. Thus, the incident flux has a maximum at about 40 meV, followed by the epithermal tail well described by the power law  $E_0^{-0.9}$ . The instrument is equipped with incident and transmitted monitors, namely  $^6\text{Li}$ -doped scintillators, for transmission measurements; 64 yttrium-aluminium-perovskite photon-sensitive detectors at front scattering angles between 33 degrees and 67 degrees and distances from the sample between 50 cm and 75 cm; and 132  $^6\text{Li}$ -doped neutron detectors at backscattering angles between 130 degrees and 163 degrees, and distances from the sample between 45 cm and 70 cm.

The energy of scattered neutrons is selected by  $^{197}\text{Au}$  analyser foils placed along the trajectory between the sample and the detectors. The analyser foil strongly absorbs neutrons of energy  $E_1 \simeq 4.9\text{ eV}$  within a narrow window, by means of a nuclear resonance and with the subsequent emission of prompt-gamma rays. The backscattering detectors work in the resonant-filter configuration using the double-difference procedure, while the front scattering detectors work in the resonant-detector configuration using the single-difference procedure [32, 33, 48, 169-174]. In addition to the analyser foil, measurements are routinely performed by cycling a second gold foil in and out of the scattered neutron trajectory between the sample and the detector. When the difference of the “in” and “out” spectra is taken, ToF spectra are obtained with the count rate corresponding to neutrons with final energy  $E_1$  only. The effect of the difference procedure is twofold: to cancel out the larger part of unwanted neutron and photon backgrounds [175-177]; and to improve the experimental resolution of the measurement. The count rates  $C_{\text{in}}(t)$  and



$C_{\text{out}}(t)$  in the two configurations are related to the difference signal  $C(t)$  by

$$(69) \quad C_{\text{out}}(t) - C_{\text{in}}(t) = C(t) + B_{\gamma}(t),$$

where  $B_{\gamma}(t)$  is a sample-dependent photon background to be corrected for [63]. By expressing the experimental counterpart of  $J(y, Q)$  (hereafter denoted as  $F(y, Q)$ ) in terms of the scattering cross sections, one obtains the expression for the single-scattering of epithermal neutrons from the sample

$$(70) \quad C(t) = \frac{E_0 I(E_0)}{Q} \left[ \frac{2}{L_0} D(E_1) \sqrt{\frac{2E_1}{m}} \Delta\Omega \right] \sum_M N_M \frac{\sigma_b}{4\pi} M F(y_M, Q),$$

where  $\Delta\Omega$  is the angular acceptance of the detector,  $N_M$  is the number of scattering centres of mass  $M$  in the sample, and  $\sigma_b$  is the bound scattering cross section.

It should be noticed that the neutron scattering cross section is in general a function of the incident neutron energy,  $\sigma(E_0)$ , ranging between the two extremes of the “bound” cross section for cold neutrons, to the “free” cross section for epithermal neutrons, as discussed in some pioneer articles by Fermi published in this journal [178]. An experimental determination of  $\sigma(E_0)$  can be obtained through neutron-transmission measurements, routinely performed at the VESUVIO spectrometer [179, 180]. The transmission of a sample is defined accordingly to Beer-Lambert law

$$(71) \quad T(E_0) = \exp(-n\sigma(E_0)d),$$

where  $n$  is the number density of the sample, and  $d$  the thickness along the direction of incident neutrons. By fixing the thickness of the sample and from knowledge of its density, the total scattering cross section can be determined experimentally. Experimental results for the transmission and cross section of liquid water and ice, at the temperatures of 300 K and 269 K, for a 2 mm thick sample are shown in fig. 9. As mentioned by Lovesey, in the IA limit the effective scattering length is that of a bound particle. This result, at first glance, may seem completely counter-intuitive in the light of the fact that in the IA limit the scattering is off a free nucleus. The derivation of this important feature, first provided by Lovesey [118], relies on the fact that, in a DINS experiment on an indirect-geometry spectrometer like VESUVIO, the intensity of the signal is proportional to the doubly differential neutron cross section. Conversely, on the same instrument the same target will yield a transmission curve defined by the total free cross section. The mathematical link between the total and doubly differential neutron cross sections is provided by the double integration procedure, with the first integral being over the energy transfer and the second over the spherical angle subtended by the detector. Performing the integration over the entire range of final neutron energies, one can note that the roots of the equation defining nuclear recoil, entering the Dirac  $\delta$ -function, present in the scattering law formulated in the IA limit, taking care of the preservation of the energy and momentum during the scattering, lead to the kinematic integral, over the total range of final energies (when converting from double to single differential cross section) which integrates out to a pre-factor  $1/[1+(m/M)^2]$ . This result forms the basis of the definition of the free cross section, namely

$$(72) \quad \sigma_f = \left( 1 + \frac{m^2}{M^2} \right)^{-1} \sigma_b.$$

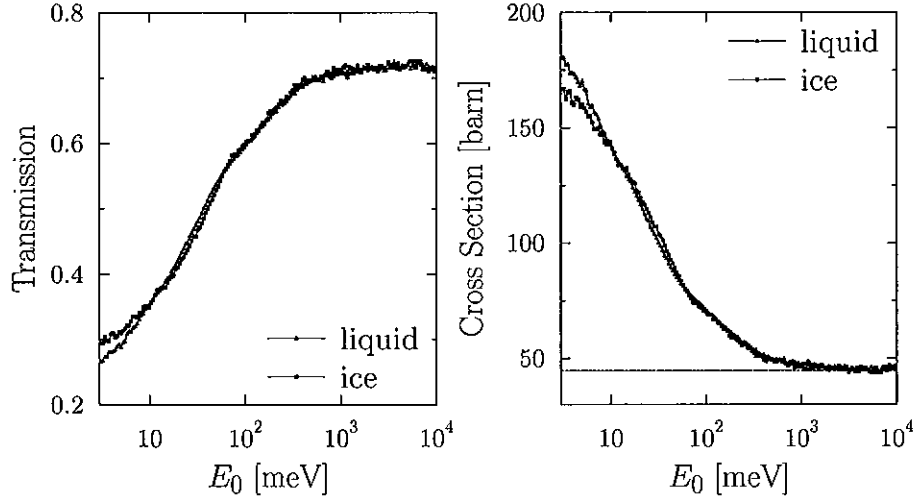


Fig. 9. – Transmission (left) and total scattering cross section (right) of a H<sub>2</sub>O sample of 2 mm thickness in the liquid (blue triangles) and ice Ih (red squares) phases.

Kinematically speaking, the extreme case is the one of the proton, characterised by a four-fold drop in its free cross section relative to the bound value. Despite the use of  $\sigma_b$  for the intensity of NCPs in eq. (70), the single-scattering limit can be achieved by noticing that the number of epithermal neutrons scattered by the sample, can be expressed in terms of the overall transmission as a Taylor expansion of the form

$$(73) \quad 1 - T(E_0 > 1 \text{ eV}) = \sum_0^{\infty} \frac{(n\sigma_f d)^n}{n!} \simeq n\sigma_f d + \frac{(n\sigma_f d)^2}{2} + \dots,$$

where the first term on the right-hand side corresponds to single-scattering events, the second term to double-scattering events, and so on. Therefore, contributions from multiple scattering are negligible if

$$(74) \quad n\sigma_f d \leq 0.1.$$

The possibility to have concurrent DINS and neutron transmission measurements on VESUVIO allows for a correct handling on the corrections for multiple scattering, as the scattering power of the sample for epithermal neutrons is experimentally determined in a simultaneous manner.

**2'6.2. Experimental resolution and fitting procedure.** In a DINS measurement, one measures an experimental NCP for each individual detector  $l$  at fixed scattering angle  $\phi_l$ , hereafter denoted as  $F_l(y, Q)$ . This quantity can be written as [31]

$$(75) \quad F_l(y, Q) = [J_{IA}(y) + \Delta J_l(y, Q)] \otimes R_l(y, Q) = J(y, Q) \otimes R_l(y, Q),$$

where  $J_{IA}(y)$  is the longitudinal momentum distribution of eq. (20),  $\Delta J_l(y, Q)$  describes the  $Q$ -dependent deviation from the IA (FSEs) introduced in eq. (26), and  $R_l(y, Q)$  [31–33] is a fixed-angle instrumental resolution function.

The convolution product,  $\otimes$ , in eq. (75) is an approximation, however its quantitative validity in the analysis of DINS data has been checked in detail in refs. [181,182]. Bearing these considerations in mind, one analyses  $F_l(y, Q)$  in order to determine the NMD and mean kinetic energy of the system under study. We also note that the use of  $J(y)$  and  $F(y)$  (and their variants) to either denote theoretical or experimental NCPs is a useful one, although the literature has not been consistent in this choice. Likewise,  $J(y)$  and  $J_{IA}(y, \hat{\mathbf{Q}})$  implicitly assume that the IA holds, whereas  $J(y, \mathbf{Q})$  does not assume the validity of this approximation.

The experimental detector-averaged NCP,  $\bar{F}(y, q)$ , is derived by calculating a simple average over the different detectors  $F_l(y, q)$ . In order to derive the  $n(p)$ , one performs a line-shape analysis of the experimental NCP  $F(y, Q)$  using a model function  $F^{th}(y, Q)$  from eqs. (19), (23) or (28) convoluted with the  $R(y, Q)$  function and corrected for FSEs. In particular, individual detectors are fitted simultaneously using  $\{\sigma_i\}$  or the coefficients in the Gauss-Hermite expansion as global fitting parameters, while other parameters as the signal amplitudes and centres are fitted separately for every detector. A least-squares fit aims at the minimisation of the  $\chi^2$  parameter defined as

$$(76) \quad \chi^2 = \sum_l \sum_i \frac{(F_l^{th}(y_i, Q_i) - F_l^{\text{exp}}(y_i, Q_i))^2}{\epsilon_{l,i}^2},$$

where  $l$  labels the detector (or subset of detectors), and  $i$  is the  $y$ -bin within each detector, respectively. As the spectra are acquired at fixed scattering angle, the value of the wave vector transfer varies for each bin of the same spectrum, and it is evaluated numerically. For each DINS measurement, the fitting parameters,  $\sigma$  and  $c_{2n}$ ,  $\bar{\sigma}$  and  $C_{2n}$ , or  $\{\sigma_i\}$  determine the  $n(p)$  or  $n(\mathbf{p})$ . The statistical errors associated to the fitting parameters are obtained from the values of the covariance matrix, including correlations between parameters from the fitting routine [31,92]. The uncertainty in the measurement of  $n(\mathbf{p})$  at some point  $\mathbf{p}$  is due to the uncertainty in the fitting coefficients  $\{\rho_i\}$ , thus having

$$(77) \quad \delta n(\mathbf{p}) = \sum_i \frac{\partial n(\mathbf{p})}{\partial \rho_i} \delta \rho_i.$$

The fitting program, after a minimum is obtained with some set of coefficients, calculates the correlation matrix  $\langle \delta \rho_i \delta \rho_j \rangle$  [183]. Hence, the variance in the NMD is

$$(78) \quad \langle \delta n(\mathbf{p})^2 \rangle = \sum_{i,j} \frac{\partial n(\mathbf{p})}{\partial \rho_i} \frac{\partial n(\mathbf{p})}{\partial \rho_j} \langle \delta \rho_i \delta \rho_j \rangle.$$

In practice, harmonic parameters are regarded as scale parameters and the errors are due to the uncertainty in the anharmonic terms.

### 3. – Atomic quantum dynamics in water, ice and amorphous ices

Some recent studies on water using DINS are presented below. This is a molecule central to both chemistry and life. The structure and dynamics of this ubiquitous molecule in the liquid phase are directly (and profoundly) influenced by quantum mechanics, not only in terms of its electronic structure and chemical bonding, but also at the level of

nuclear motions. NQEs include ZPEs, tunnelling across hydrogen bonds (HBs), anomalous ionic conductivity, intriguing isotope effects in its thermodynamic properties, and large deviations from MB behaviour for both the average nuclear kinetic energy  $\langle E_K \rangle$  of individual nuclei and their associated NMDs. Internal modes like vibrations are highly quantized, and while those modes can be treated with rigid constraints or simple classical models due to their small amplitudes of motion, the shortcomings of such an approach are evident as their strengths and amplitudes are sensitive to the interplay between the HB-induced mechanical anharmonicity and the ground-state atomic dynamics. Liquid water shows quantum effects which are of relevance for biological molecules in solution, as it is particularly evident through the observation of quantum effects on reaction rates in enzymes.

As one would naively anticipate on qualitative grounds, at the atomic scale, these effects are most prominent for the proton, owing to its light mass. Recent DINS work has also established that NQEs can also be of key importance to explain the dynamics of the heavier O atom. As stressed earlier in this work, DINS observables provide unique information on the underlying potential energy surface that individual nuclei see as the local environment evolves, as, for instance, in the presence of proton tunnelling, delocalisation, and bond breaking.

Water is the most important hydrogen-bonded liquid, and thus it has been studied in great detail experimentally using several spectroscopic techniques. Its structural and dynamical properties play a central role in many phenomena of relevance to different areas of science, in fundamental and applied science. These can be attributed to the ability of water molecule to establish a dense but still very dynamic three-dimensional network of hydrogen bonds (HB)s, connecting adjacent molecules, in which both the number and the strength of the hydrogen bonds continually fluctuate. The 3D hyperdense flexible HB network in liquid water is at the origin of its exceptional physical and chemical properties [1]. The absolute values of the enthalpy of formation,  $\Delta H$ , of an HB, is in the range 5 kT to 10 kT at 300 K (weak H-bond), thus the corresponding H-bonded complexes are relatively robust at room temperature although they exhibit flexibility: they can easily undertake reversible disruption or transformation, with capacities of evolution and adaptability and can be disrupted with the energy provided by thermal fluctuations. A decrease in temperature from liquid water to ice results in a much stiffer HB network, thus ice, with its dense and rigid HB network, does not exhibit so many exceptional properties and is no longer a life-supporting medium. In opposition, that of liquid water is flexible, due to the possibilities for each  $H_2O$  to perform large-amplitude librations. The exceptional presence of a hyperdense HB network gives it unique possibilities to accommodate embedded molecules, making water an exceptional liquid to solvate ions, organic molecules, or to give with them original molecular structures, such as micelles of detergents, biological membranes made of phospholipid bilayers, or Langmuir-Blodgett films. A comprehensive description of these properties requires an accurate model of water and HB.

Intermolecular chemical interactions occurring in bulk water represent small changes in the energy of constituents, compared to the ZPE of protons. Thus, in water, the proton NMD at typical temperatures is due almost entirely to ZPE. Nearly all simulations of water in a variety of settings are done with models of water for which these changes cannot occur, or if they can, are not considered because of the additional expense in treating the protons quantum mechanically. In water, the ZPE does change, however, as the structure of the HB network changes. As a result, NQEs in aqueous media can be very significant even at ambient conditions, and are known to affect in a fundamental way a variety of phenomena. For example, the pH of liquid water depends strongly on

isotopic substitution: it goes from 7.0 to 7.4 upon deuteration, and to 7.6 upon tritiation. Extrapolation of this trend to the classical limit of nuclear motions (*i.e.*, infinite mass), the  $pH$  of water would be 8.5, that is, a thirty-fold change in the equilibrium acid-base dissociation constant [9]. Moreover, the water molecule is also known to control reactivity in biological media, as shown by the large variations on molecular and biomolecular stability upon H/D substitution [184, 185]. The HB network in water is flexible at room temperature, while a decrease in temperature from liquid water to ice results in a much stiffer HB network [1]. The end result is that ice loses several of the exceptional properties of liquid water and is no longer a life-supporting medium. The origin of this flexibility in liquid water can be traced back to large librational excursions that  $H_2O$  molecules can perform, without breaking the HB network, a possibility that classical methods to describe ordinary liquids have great difficulties taking into account. Historically, the description of these dynamic properties can be traced back to infrared and Raman studies of vibrational spectra, followed by more recent neutron investigations. The effects associated with anharmonicity and NQEs naturally emerge when interpreting the exceptional spectroscopic properties of HBs, in an attempt to understand which bonding motifs constitute the primary path through which protons can be transferred across molecules at the nano- to mesoscale.

The development of the VESUVIO instrument and DINS has enabled direct observations of the quantum ground state of the protons in water under a variety of conditions, including confinement. As far as water is concerned, DINS is currently a quantitative and well-established technique capable of probing  $n(p)$  and obtain fresh insights into the intermolecular HB interactions at the heart of the peculiar properties of water, in many respects complementary to INS and optical spectroscopy [7, 110]. DINS images the quantum ground state of the protons (or the deuterons) and associated NQEs. This is the case in molecular phases in which molecules fluctuate but remain intact entities. In some cases the proton delocalises, appearing to be in potential wells that are either flat-bottomed or double wells, in others, where it becomes more localised. The energy changes associated with changes in the ZPE of the protons can be large on the scale of  $k_B T$  and are also significant for chemi- and physisorption. The  $n(p)$  is an ideal physical quantity to test our understanding of how water adapts its HB network in the solid, metastable, stable and supercritical phases. Thus, in a DINS experiment one observes the changes in ZPE directly as well as the sensitivity of the NMD to the shape of the proton confining potential, provided one bears in mind the need of including charge-overlap effects, or covalence with the oxygen acceptor, in order to adequately describe it. The changes in  $\langle E_K \rangle$  can be large ( $> k_B T$ ), and occur in either direction. In liquid and polycrystalline materials, DINS accesses only the spherically averaged NMD, while the directional NMD is accessible in DINS measurements on single crystals. To this end, it is worth while stressing some of the general features of NMD line shapes of H and O in water and ice that DINS can highlight: the high-momentum tail of the distribution is determined by the highest-frequency mode of vibration, the stretch mode, with the proton moving along the bond. The measured NMD is an isotropic average of the individual proton distributions, but the stretch mode dominates at high momenta.

These issues have been the main motivations of a considerable amount of measurements and theoretical work on liquid water in the last 15 years. Since early measurements, a variety of DINS work of the proton mean kinetic energy in bulk liquid water, from the supercooled metastable phase to supercritical conditions, and in confined water, is now available in the literature (see [31-33]). These studies highlight the connection between the proton short-scale response to the changes in the HB network [49, 93, 113, 186-194],

and show evidence of NQEs which determine strong deviations of the measured NMD from MB predictions (see fig. 1). In the last years, DINS has also stimulated the development of comprehensive microscopic models to account for the properties of water and water-based systems. In particular, the existing literature shows a significant expansion of new many-body techniques addressing NQEs on hydrogen-bonded systems, computer models addressing the study of water, interfacial water and hydration using empirical and polarizable models [193], open Path Integral Molecular Dynamics [113, 195, 196] and open Path Integral Car-Parrinello Molecular Dynamics (PICPMD) performed on phases of high pressure ice [197, 198]. In these cases, the ZPE can be modelled in terms of quantized harmonic modes to a first approximation. Often the approximation of effective spherical harmonic oscillators is further made. The limits of these approximations are, however, borne out by several experimental observations such as *e.g.*, in DINS experiments, which show both directional effects and anharmonicity. Anharmonicity is also revealed by the isotope dependence of phase-transition temperatures upon proton/deuteron substitution. Disentangling directional and anharmonic effects is crucial to better understand the molecular structure and dynamics, but is a difficult task in experiments that measure average material properties. In this context, *ab initio* molecular dynamics (AIMD), and PI simulations, have proven to be a valid complement to experiment and have led to successful interpretation of several of the observations mentioned above. It should be stressed, with the exception of diffraction, that experiments usually measure dynamical properties that are not directly accessible by statistical simulations at equilibrium. However, in many cases, such as with DINS and other spectroscopies, the separation of time scales between the probe and the equilibrium dynamics of the system makes direct comparison with PI simulations a very useful tool. While often anharmonicity manifests itself as a correction, albeit important, to a dominantly harmonic motion, there are cases in which the harmonic model should be dismissed altogether. This situation occurs when localisation in a single potential well is no longer the paradigm and the protons delocalise by tunnelling across more than one site. A dramatic manifestation of this phenomenology is provided by quantum-phase transitions, *i.e.*, transitions between different equilibrium structures that are driven by quantum fluctuations. Examples of these include potassium dihydrogen phosphate and water ice at high pressure. Under appropriate thermodynamic conditions, these transitions are characterised by large isotope effects that can only be accounted for if tunnelling plays a major role. The presence of sporadic tunnelling effects at low temperatures has been inferred in experiments even in situations dominated by quasi-harmonic ZPEs. However, unambiguous experimental evidence of tunnelling phenomena is still missing in these cases and remains a matter of current and intense research.

In the following subsections, we provide a review of experimental investigations of NQEs in water systems using electronvolt neutron spectroscopy. These works include light and heavy liquid water as well as ordered and amorphous ices, both archetypes of condensed-matter HB systems. These examples emphasise the experimental progress beyond the measurement of fundamental observables such as  $\langle E_K \rangle$  and  $n(p)$ , and include the ability of DINS to explore the directional components of the mean kinetic energy tensor,  $\langle E_K \rangle_{x,y,z}$ , of light and heavy nuclei, and to highlight the existence of competing NQEs [199]. These selected examples aim at illustrating the continuous development taking place as the scope and applicability of the DINS technique expands into new areas to cover light and heavy species, as well as its use along with contemporary materials modelling.

**3'1. Water across the melting point.** – As hydrogen is the central piece of the HB puzzle, NQEs in water play a critical role up and above ambient temperature and are known to be relevant in charge-transfer mechanisms and acid-base chemistry. Theoretically, many models and computational approaches encounter difficulties in reproducing the large librational excursions that liquid water can undergo without breaking the HB network. In several theoretical approaches, the relatively minor intermolecular quantum effects in a water-like liquid have been considered to be generally amenable to approximation, while the most recent works show that the details of the NMDs have an influence to the intermediate-range order properties of the HB network. A recent joint study based on DINS measurements and PIMD simulations [92] is reported as an example below of how fully quantum-mechanical simulations are needed in order to explain NQEs.

Experimental data on heavy water and ice,  $D_2O$ , across the melting point and at room temperature were obtained on VESUVIO. As a first qualitative remark, the values of the kinetic energy  $\langle E_K \rangle$  of both the D and O atoms were found to be well above the MB value of  $\frac{3}{2}k_B T \sim 38 \text{ meV}$  at  $T = 300 \text{ K}$ . This can be illustrated by recalling eq. (57) and the introduction of an effective temperature to explain the broadening of an otherwise Gaussian line shape. However, deviations from a Gaussian NMD were found in the data. The latter were modelled with an anisotropic NMD of the form of eq. (38), where the three parameters of the fit,  $\sigma_\alpha$  with  $\alpha = 1, 2, 3$ , describe the anisotropy of the momentum distribution and the confining potential in three orthogonal directions. From this equation it can be noted that, even if the anisotropic NMD has an explicit dependence on the momentum as a vector, the line shape obtained in a DINS experiment where the sample is disordered needs to be averaged over all possible orientations, as implied by the angular average  $\langle \dots \rangle_\Omega$ . It can be shown that anisotropy on a NCP appears as an oscillatory deviation from a Gaussian line shape [146] that can then be spotted on good-quality data. For each value of  $\sigma_\alpha$ , a contribution to the mean kinetic energy can be defined as

$$(79) \quad \langle E_K \rangle_\alpha = \frac{\hbar^2 \sigma_\alpha^2}{2M}, \quad \sum \langle E_K \rangle_\alpha = \langle E_K \rangle.$$

Table I shows the results from the aforementioned study with the values of the mean kinetic energy of D and O, as well as the directional contributions obtained via a fit using eq. (38). Results from both experiment and simulation are reported. A marked anisotropy is found as  $\sigma_z > \sigma_y > \sigma_x$  and a satisfactory degree of agreement is found between theory and experiment. In the case of the computer simulation, for water molecules changing orientation with time in the liquid phase, the Transient Anisotropic Gaussian (TAG) approximation was used [12] using a running average of the kinetic-energy estimator in a triangular averaging window of 100 fs. Otherwise, in the approximation where the principal axes of the kinetic energy tensor are on average aligned with respect to the geometry of the molecule, one can accordingly rotate the kinetic-energy estimator using the mean-square displacement (MSD). On the experimental side, the model of eq. (38) is based on the assumption that the correlation amongst the motion along the three axes is negligible. Therefore, one does not have an *a priori* orientation of the frame of reference with respect to the molecule. Common practice is to define the  $x$ -axis in the direction perpendicular to the plane of the molecule, and the  $z$ -axis along the OH-bond direction, even if a small rotation of the  $yz$ -plane can be expected as coupling between stretch and bend modes increases.

TABLE I. – Comparison between theoretical and experimental components of the quantum kinetic energy for D and O in heavy water, at different temperatures. All values are in meV, and the theoretical results have a statistical error bar below 0.1 meV. We also report the computed centre-of-mass mean kinetic energy  $\langle E_{\text{COM}} \rangle$  of the D<sub>2</sub>O molecules. Results adapted from ref. [92].

|                                       | D [exp]        | D [TAG/MSD] | O [exp]        | O [TAG/MSD]                             |
|---------------------------------------|----------------|-------------|----------------|---|
| D <sub>2</sub> O, $T = 300$ K, liquid |                |             |                | $\langle E_{\text{COM}} \rangle = 42.1$ |
| $\langle E_x \rangle$                 | $20.1 \pm 1.1$ | 19.5/18.9   | $15.8 \pm 1.7$ | 13.6/13.7                               |
| $\langle E_y \rangle$                 | $36.1 \pm 2.3$ | 26.1/25.6   | $19.5 \pm 1.3$ | 19.4/20.4                               |
| $\langle E_z \rangle$                 | $55.1 \pm 2.3$ | 64.6/65.7   | $26.3 \pm 1.5$ | 23.4/22.3                               |
| $\langle E_K \rangle$                 | $111.3 \pm 3$  | 110.2       | $61.6 \pm 3.1$ | 56.4                                    |
| D <sub>2</sub> O, $T = 280$ K, liquid |                |             |                | $\langle E_{\text{COM}} \rangle = 39.5$ |
| $\langle E_x \rangle$                 | $18.8 \pm 1.1$ | 19.4/18.9   | $16.0 \pm 2.3$ | 13.6/13.7                               |
| $\langle E_y \rangle$                 | $38.6 \pm 2.5$ | 25.7/25.2   | $21.0 \pm 0.6$ | 19.2/20.2                               |
| $\langle E_z \rangle$                 | $54.2 \pm 2.4$ | 63.6/64.6   | $24.1 \pm 2.1$ | 23.2/22.2                               |
| $\langle E_K \rangle$                 | $111.6 \pm 2$  | 108.7       | $61.1 \pm 3.1$ | 56.1                                    |
| D <sub>2</sub> O, $T = 274$ K, solid  |                |             |                | $\langle E_{\text{COM}} \rangle = 39.2$ |
| $\langle E_x \rangle$                 | $22.5 \pm 1.8$ | 20.1/19.8   | $16.1 \pm 2.3$ | 13.7/13.8                               |
| $\langle E_y \rangle$                 | $37.4 \pm 2.5$ | 26.3/25.9   | $20.1 \pm 1.6$ | 19.0/19.9                               |
| $\langle E_z \rangle$                 | $48.1 \pm 3.4$ | 61.9/62.4   | $24.2 \pm 1.4$ | 23.0/21.9                               |
| $\langle E_K \rangle$                 | $108.0 \pm 2$  | 108.3       | $60.4 \pm 4$   | 55.7                                    |

The PIMD simulation predicts an opposite trends for the  $x$ - and  $z$ -contributions to  $\langle E_K \rangle$ , and these are qualitatively confirmed by the experimental data. The change of internal contributions leaving the overall value of the mean kinetic energy unchanged is known as “competing NQEs” and it is a mechanism found beyond the water molecule and in many systems exhibiting HB (see below). The use of eV neutron spectroscopy allows to measure the competing NQEs and to explain how these cause a subtle interplay of water’s NQEs and their manifestation in the values of  $\langle E_K \rangle$ . This principle has recently been used to explain the known anomalies in water associated with isotope substitution. Likewise, competing NQEs have been qualitatively explained in the case of H<sub>2</sub>O as it crosses the melting [110] via comparison to INS data. Figure 10 reports the analysed data for the case of liquid water and ice, showing opposite shifts in librational band positions relative to the stretch mode. As the HB gets stronger in the solid phase as opposed to the liquid, departures from relatively unhindered rotations are more pronounced, and librational frequencies increase as the HB networks becomes stronger. Conversely, stronger intermolecular O...H interactions compete with covalent bonds within the molecule and lower the stretch frequency as a consequence of the broadening of the potential along the OH...O direction.



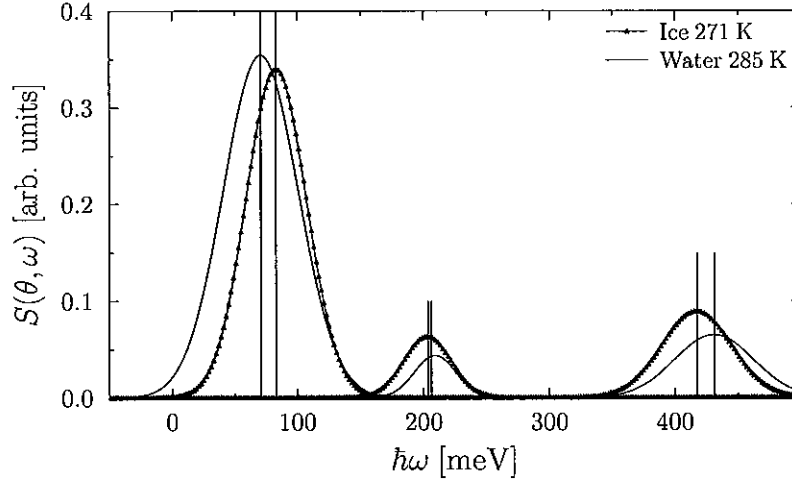


Fig. 10. – Fits on the INS data presented in ref. [110] in the case of liquid water (blue) and ice (red) at a scattering angle  $\theta \sim 20$  degrees. Shifts of the librational, bending and stretching frequencies across the phase transition are highlighted by vertical lines.

As the value of  $\langle E_K \rangle$  can in principle be obtained from the VDOS (neglecting anharmonic contributions), one can express the change in the kinetic energy as

$$(80) \quad \Delta \langle E_K \rangle = \frac{3}{4} \int_0^\infty \frac{E}{4} \Delta g_H(E) dE \sim \Delta E_{\text{lib}} + \Delta E_{\text{str}}.$$

This result only holds when all the modes of vibration in the ground state (within the harmonic approximation) are considered, as the population factor has been omitted from the integrand.

**3.2. The triple point of water.** – Recent INS studies of ice and water in stable and metastable states in the vicinity of the triple point show that the OH stretching component of  $\langle E_K \rangle_z$  has almost identical values when interpreted within a harmonic framework: 98 meV, 100 meV and 100 meV for ice at 271 K, supercooled water at 271 K, and liquid water at 300 K, respectively [7]. This is an indication that NQEs associated with the OH stretching frequency,  $\omega_z$ , are weakly temperature-dependent in the explored temperature range. This work has also shown that DINS measurements allow to go beyond the harmonic framework and can provide full directional components of the mean kinetic-energy tensor [94].

A recent DINS study in the metastable phase of water (and ice) at  $T = 271$  K (*i.e.*, near the triple point), and liquid water at 300 K, provide accurate measurements of the proton  $n(p)$  and its associated directional mean kinetic energy components  $\langle E_K \rangle_\alpha$  [95]. The measurement on ice was specifically recorded at the same temperature as on supercooled water, in order to allow a quantitative benchmark with previous DINS experiments performed at the same thermodynamic state point [93]. Values for  $\sigma_\alpha$  from this experiment are reported in table II. These highlight a main distinctive feature between supercooled water and ice at  $T = 271$  K: the anisotropy of the proton NMD is slightly more pronounced in supercooled than in the solid phase. Similar features have

TABLE II. –  $\langle E_K \rangle$  and individual  $\langle E_K \rangle_\alpha$  values in bulk supercooled water (SW) and ice at  $T = 271$  K. For each sample, a simultaneous fit of experimental  $F_l(y, Q)$ 's is accomplished using two parametric models for  $n(p)$ : (a) a model-independent line shape (cf., M1, eq. (35)); and (b) a 3D anisotropic Gaussian line shape, M2, derived from a quasi-harmonic model, (cf. eq. (38)). These are obtained using the model of eq. (38), while the model-independent line shape gives  $\langle E_K \rangle$ ,  $c_4$  and  $\sigma$ . The latter is found to be equal to  $\bar{\sigma} = \sqrt{\sum \sigma_\alpha^2 / 3}$  where values for  $\sigma_\alpha$  are taken from the model of eq. (38) [95]. Results taken from ref. [95].

| $T$                     | [K]                | SW<br>271       | Ice<br>271      | Ice [93]<br>271 |
|-------------------------|--------------------|-----------------|-----------------|-----------------|
| <b>M1</b>               |                    |                 |                 |                 |
| $\sigma$                | [Å <sup>-1</sup> ] | $5.01 \pm 0.02$ | $5.03 \pm 0.03$ | $5.01 \pm 0.03$ |
| $c_4$                   |                    | $0.11 \pm 0.01$ | $0.11 \pm 0.02$ | $0.10 \pm 0.01$ |
| $\langle E_K \rangle$   | [meV]              | $156.0 \pm 2.0$ | $157.0 \pm 2.0$ | $156.0 \pm 2.0$ |
| <b>M2</b>               |                    |                 |                 |                 |
| $\sigma_x$              | [Å <sup>-1</sup> ] | $2.9 \pm 0.5$   | $3.7 \pm 0.1$   | $3.7 \pm 0.3$   |
| $\sigma_y$              | [Å <sup>-1</sup> ] | $5.0 \pm 0.5$   | $4.3 \pm 0.3$   | $4.3 \pm 0.4$   |
| $\sigma_z$              | [Å <sup>-1</sup> ] | $6.5 \pm 0.2$   | $6.6 \pm 0.2$   | $6.5 \pm 0.4$   |
| $\langle E_K \rangle_x$ | [meV]              | $17 \pm 5$      | $28 \pm 2$      | $29 \pm 4$      |
| $\langle E_K \rangle_y$ | [meV]              | $52 \pm 10$     | $38 \pm 5$      | $38 \pm 9$      |
| $\langle E_K \rangle_z$ | [meV]              | $86 \pm 5$      | $91 \pm 5$      | $87 \pm 9$      |
| $\langle E_K \rangle$   | [meV]              | $156.0 \pm 2.0$ | $157.0 \pm 2.0$ | $154.0 \pm 2.0$ |

also been obtained in a combined INS-DINS investigation of water at  $T = 285$  K and ice at  $T = 271$  K [110]. Values of the proton total mean kinetic energy,  $\langle E_K \rangle = 3 \frac{\hbar^2 \sigma^2}{2m}$ , and the directional components along the three axes,  $\langle E_K \rangle_\alpha = \frac{\hbar^2 \sigma_\alpha^2}{2m}$ , were derived for ice, supercooled water, and water at room temperature, as well as compared with values obtained from INS [7] and theory [200]. In this case,  $\langle E_K \rangle$  for ice at  $T = 271$  K together with the  $\sigma_\alpha$  values, are the same within experimental uncertainties to those obtained in previous measurements at the same temperature [93]. This represents a reference benchmark which validates and strengthens the total value of  $\langle E_K \rangle = 156$  meV, and its directional  $\sigma_\alpha$  components obtained for supercooled water. Here, the transition from a disordered, metastable phase (supercooled water) to a polycrystalline one (ice) is evinced by the competition between the directional energy components  $\langle E_K \rangle_\alpha$ , so as to produce a subtle cancellation effect, resulting in very similar values for  $\langle E_K \rangle$  [19].

**3'3. Water under supercritical conditions.** – Supercritical water is of relevance in applications as varied as producing hydrogen from glucose [201], the fabrication of YAG nanoparticles [202], or SuperCritical Water-cooled Reactors, promising candidates for Generation-IV nuclear-power stations [203]. As for all supercritical fluids (SCFs), small changes in pressure or temperature in water result in large variations in solubility. This allows the production of fine particles via precipitation of a solute from supercritical solution by rapidly exceeding the saturation point of the solute by dilution, antisolvent,

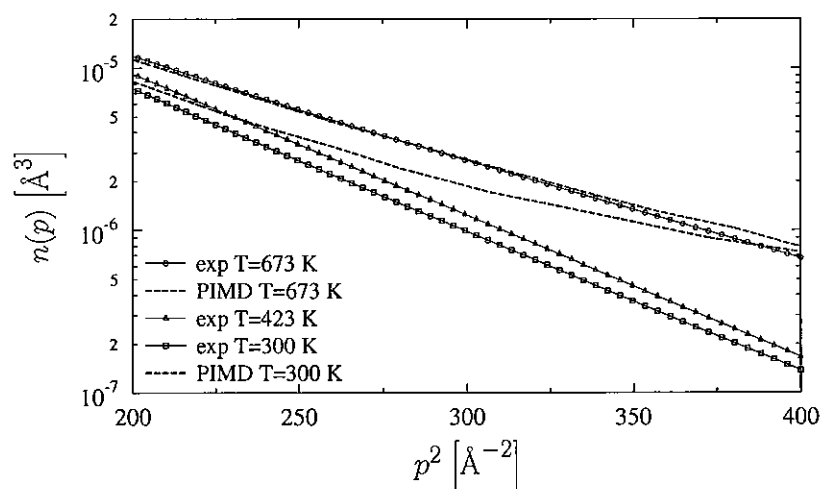


Fig. 11. – Proton NMDs in the region where they are dominated by motions along the O-H stretch direction:  $T = 673$  K (red circles),  $T = 423$  K (brown triangles), and  $T = 300$  K (blue squares).

depressurization, or attemperation [204]. In addition to the above properties of SCFs, supercritical water (SCW) exhibits peculiar properties due to the presence of intermolecular HBs. In SCW, more than 70% of HBs are destroyed to a non-polar dimer, and further decomposed to monomer,  $H^+$  and  $OH^-$  ions. Thus, SCW becomes a weakly polar solvent that can dissolve non-polar organics to produce fine particles via precipitation. On the other hand, high concentrations of  $H^+$  and  $OH^-$  ions provide both basic and acidic reaction conditions for the synthesis of novel materials. Figure 11 shows a number of experimental and theoretical results on supercritical water obtained over the past decade. The calculated PIMD distribution at 673 K (red dashed line) is in very good agreement with the measured results and is nearly identical to that of the free monomer. The calculated result at 300 K (blue dashed line) gives too large a momentum width to describe the experimental data [113]. The variation of water's properties as it is heated under pressure to reach the supercritical point and above provides a means of investigating the extent and nature of the HB network on those properties as this network is pulled apart.

The structure of water near the supercritical point is still a matter of controversy [205]. The proton dynamics of SCW was first fully characterized by DINS measurements performed from room temperature and pressure up to above the supercritical point [113,187]. From this study the shape of the proton NMD in water has been derived and compared with theoretical calculations based on a polarizable water model [206]. The line shape of  $n(p)$  in SCW was obtained using eq. (38). The results show a transverse-momentum width slightly more than one half of the intrinsic width along the OH-stretch direction. The  $n(p)$  line shape along the HB direction is narrower in the dense phases and approaches that of the isolated molecule in the more dilute phases. The tail of the NMD arises from the momentum along the bond direction. The orientationally averaged NMD is reported in fig. 11 and discussed below.

Since the proton is most tightly bound along the covalent-bond direction, and tight binding implies wide momentum widths, it is clear that this width has increased, which

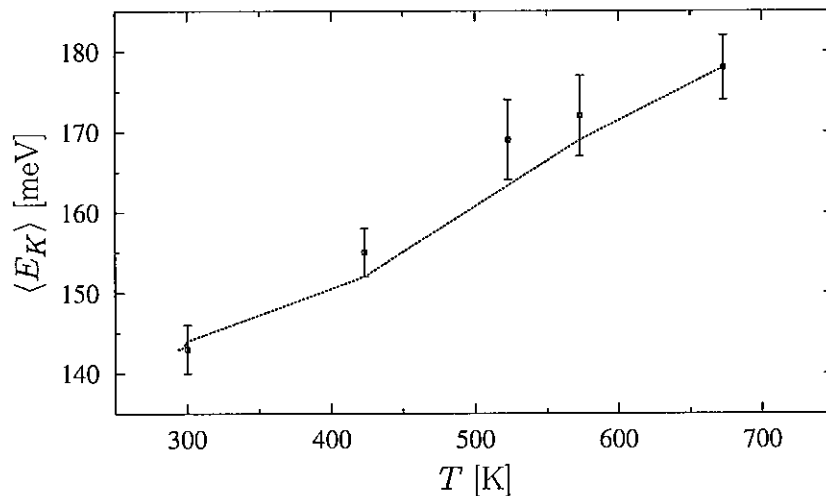


Fig. 12. – Temperature dependence of the proton mean kinetic energy for the stable liquid and supercritical water (blue squares with error bars, taken from refs. [113,190,208]). The theoretical predictions from Moreh *et al.* [209] are shown as a red dotted line.

can be interpreted as arising from a slight increase in the average HB distance in water, so that the proton becomes more tightly bound to its covalently bonded and neighbouring O atom. The change in line shape reflects changes in HB and is easily observable, the difference being significant and well beyond experimental uncertainties. Changes in covalent-bond lengths are only 4% [2], and the DINS measurements are clearly accurate enough to see the dynamical consequences of this subtle shift. The calculated NMD at 673 K is in very good agreement with the DINS results and is nearly identical to that of the free monomer. The theoretical model, which includes only electrostatic interactions, is unable to explain the softening of the local potential experienced by the protons in the dense phases, although it accurately predicts the NMD for the dilute phases, suggesting that covalency with the H-bonded O plays a significant role in determining the surrounding potential-energy surface. Evident structural changes in going from ambient to high temperatures approaching the supercritical state are also readily discernible in fig. 12 [113].

Notwithstanding the above, a complete picture is far from being clear, as the interpretation of structural data is often carried out in terms of water as a collection of monomers interacting electrostatically. The comparison of NMDs of aqueous protons obtained from DINS [113] with those calculated from two electronic-structure-based models show that below 500 K, these electrostatic models, one based on a multipole expansion including monomer polarizability, are not able to even qualitatively account for a sizeable ZPE contribution to the enthalpy of vaporization [207]. This discrepancy provides strong evidence that the change in the proton NMD upon solvation cannot be entirely explained by electrostatic effects alone, but requires correlations of the electronic states on the molecules involved in HB to produce the observed softening of the potential. At present, the vast majority of models and empirical potentials can account for the experimental structure factors of water [210,211], yet they fail to reach the requisite level of accuracy to describe proton NMDs quantitatively. Indeed, a 10% change in the ground-state kinetic energy, which is very large on the scale of experi-

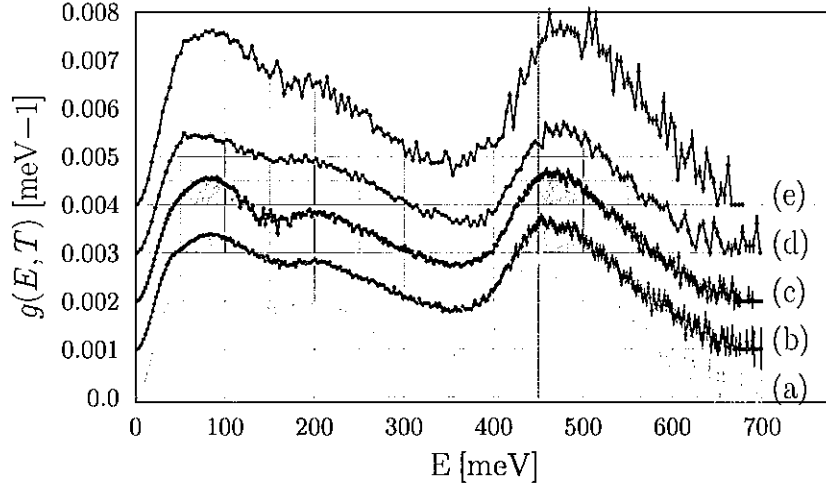


Fig. 13. – Vibrational densities of states  $g_H(E)$  at (a) 553 K; (b) 623 K; (c) 663 K; (d) 733 K and (e) 823 K. Spectra have been normalised to unity and vertically shifted by  $0.001 \text{ meV}^{-1}$  to ease the visualisation [212].

mental uncertainties (less than 1%), amounts to a change in the width of the proton wave function by only  $5 \times 10^{-3} \text{ \AA}$ . This would make an indiscernible difference in the structure factors, where the scale length of the relevant features is about  $1 \text{ \AA}$ . Given that the proton NMD is a function of the underlying potential, Burnham *et al.* [207] have pointed out that intermolecular perturbations of the proton potential in the bulk phases of water cannot be satisfactorily modelled using only classical electrostatics models. As evidenced by comparison with experiment, there appears to be an additional softening of the proton potential upon HB formation beyond that captured by these electrostatic models.

A common description of the SCW phase is based upon the subdivision of the water phase diagram into liquid-like and vapour-like regions. The border line between the two subregions is defined in several ways, as for example the locus of specific-heat maxima starting at the critical point. To this aim, in a recent experiment, DINS and INS techniques have been used in combination with microscopic models that account for the changes in chemical bonding as a function of temperature and pressure in the supercritical phase. The experiment was performed in the temperature range  $553 \text{ K} < T < 823 \text{ K}$  (above and below  $T_C$ ) at the constant pressure  $P > P_C$ , where  $T_C$  and  $P_C$  are the critical temperature and pressure, respectively. The phases investigated included subcritical, liquid-like and gas-like SCW. The experimental results show that the most important contribution to the scattering law comes from excited librational and stretching modes, whose existence reflects the persistence of HB at all the temperatures investigated [212]. Figure 12 reports the proton mean kinetic energy over a temperature range from the stable liquid to supercritical water. Figure 13 shows the hydrogen-projected VDoS obtained from INS measurements. Three main contributions are observed: the librational modes (less than  $100 \text{ meV}$ ), the bending mode (around  $200 \text{ meV}$ ), and the stretching mode (between  $450$  and  $473 \text{ meV}$ ).

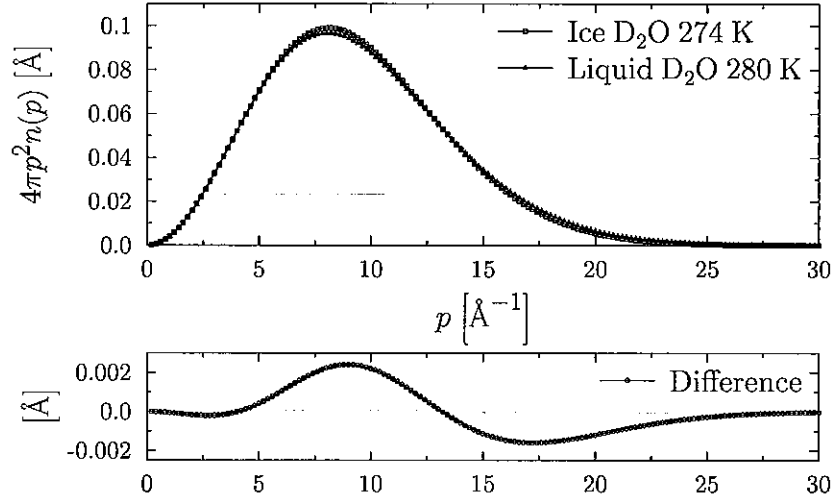


Fig. 14. – Radial  $n(p)$  for D in solid heavy water at  $T = 274 \text{ K}$  (red continuous line) and the liquid at  $T = 280 \text{ K}$  (blue continuous line). The difference of the two spectra is shown in the lower panel.

**3.4. Heavy water and quantum melting.** – As shown previously, even though intrinsic NQEs can be very large (the ZPE of an O-H stretch mode, *i.e.*,  $\frac{1}{2}\hbar\omega$ , is in excess of 200 meV relative to classical predictions), it is often the case that their net effect on macroscopic properties can be relatively small. Sometimes, NQEs compete with each other and partially cancel each other out. This phenomenon is thought to play a role in determining the melting and boiling temperatures of water. For instance, the melting temperatures of light and heavy water differ by less than 4 K, and the boiling temperatures by just 1 K. From some recent theoretical work [199,213], there are indications that these effects stem from a partial cancellation of NQEs associated with the intra- and intermolecular components of the HB, so that the net effect is small even if the individual contributions are quite large. In particular, the competition between NQEs can be seen very clearly when decomposing changes in the quantum kinetic energy of protons and deuterons along different molecular axes [156,214].

Competing NQEs, recently proposed in a variety of simulation work [156,199,213,214], are likely to be at the root of the explanation as to why many of the properties of water depend rather mildly upon isotopic composition. Even at room temperature, quantum mechanics plays a major role in determining the quantitative behaviour of H and D nuclei in water, changing significantly the values of physical properties such as the heat capacity. The first direct experimental observation of competing NQEs on both light and heavy water has been observed in both heavy water and ice [92,145] (cf. fig. 14, and table I). DINS investigations supplemented by PIMD simulations provide the anisotropy of the mean kinetic energy tensor  $\langle E_K \rangle_\alpha$ . Results show that the largest two components of  $\langle E_K \rangle$  partially cancel each other out resulting in a small net effect on the melting and boiling points of water [145]. The most interesting feature in  $\langle E_K \rangle$  is observed upon freezing. A small change in the  $\langle E_K \rangle$  during the melting process corresponds to the greatest changes of its internal components, namely the  $x$  and  $z$  components of  $\langle E_K \rangle_\alpha$ . These changes happen along different directions, giving rise to a global cancellation: the

increase of the  $x$ -component may be interpreted in terms of more hindered librations in the solid phase; a decrease along  $z$  may be interpreted as a red shift of OH stretching due to an increase in HB, *i.e.*, the weakening of covalent OH bonds as seen in the vibrational data. Both NMD line shapes across the melting point of  $D_2O$  have a very similar second moment, yielding kinetic energies of  $108.3 \pm 2.0$  meV in the solid at  $T = 274$  K, and  $111.3 \pm 3.0$  meV in the liquid at  $T = 280$  K, respectively. Nonetheless, the differences shown in their shapes reflect directly changes in the directional components of the mean kinetic energy in the two phases discussed above.

In conclusion, it is interesting to see how, despite the noticeable differences in the individual values of  $\langle E_K \rangle_\alpha$ , the theoretical and experimental  $n(p)$  line shapes for D are almost indistinguishable. The computed  $n(p)$  depends only weakly on how the kinetic energy components are distributed, yet in a more pronounced way on the total  $\langle E_K \rangle$ .

**3'5. Amorphous ices.** – Ice is the prototypical HB material, displaying a great structural complexity in terms of crystalline polymorphs and amorphous forms. At present we know that there are sixteen crystalline and at least two families of amorphous forms of ice [215-217]. All the amorphous forms of ice are always metastable with respect to related crystalline phases and preserve approximately tetrahedral HB arrangements. It has been shown that low-density amorphous ice (LDA), unannealed high-density amorphous ice (uHDA), and very-high-density amorphous ice (vHDA) are structurally distinct with respect to the number of interstitial water molecules in the first coordination shell. Indeed, these structural differences manifest themselves in bulk densities of  $0.94 \text{ g cm}^{-3}$  (LDA),  $1.15 \text{ g cm}^{-3}$  (uHDA) and  $1.26 \text{ g cm}^{-3}$  (vHDA) at ambient pressure and 77 K [217, 218]. A number of open questions need to be addressed in the context of the amorphous ices. These are related to issues such as what exactly constitutes a distinct amorphous state, the dynamics and potential glass transitions, as well as the suggested existence of a liquid-liquid critical point in the phase diagram. In many respects, this reflects how our understanding of water at low temperatures is still incomplete. As well as in the case of liquid water, the microscopic properties of all amorphous forms of ice are strongly influenced by quantum-mechanical effects. A recent DINS study combined with INS and Raman scattering has provided new information on the anisotropic nature of proton motions in amorphous ices, LDA, uHDA, and vHDA, at 80 K and ambient pressure [94].

Figure 15 shows the angle-averaged  $F_l(y, Q)$  function,  $\bar{F}(y, Q)$ , for vHDA at 80 K. Data of similar quality have been obtained for LDA and uHDA as well. The experimental  $n(p)$  lineshapes for the amorphous ices shown in fig. 15 have been determined by modelling the NMDs as spherical averages of multivariate Gaussians. The mean kinetic energies of the protons are found to increase with increasing density, indicating the weakening of hydrogen bonds as well as a trend towards steeper and more harmonic potential, as suggested by the results summarized in fig. 18. DINS shows much more pronounced changes in the O-H stretching component of the mean kinetic energy going from low- to high-density amorphous ices than indicated by INS or Raman spectroscopy. The peak positions of stretching, bending and librational modes from INS and Raman spectra of the amorphous ices are summarized in figs. 17 and 16. Notable trends include blue shifts of the O-H stretching bands and the red shift of the librational band going from LDA to uHDA (or HDA) and vHDA. This trend highlights the power of the DINS technique to retrieve accurate ground-state kinetic energies beyond the harmonic approximation. Results show the pronounced softening of the effective stretching potential in LDA compared to the HDAs. As the HB weakens with increasing density, the curvature of the effective potential increases and its shape becomes similar to the shapes inferred

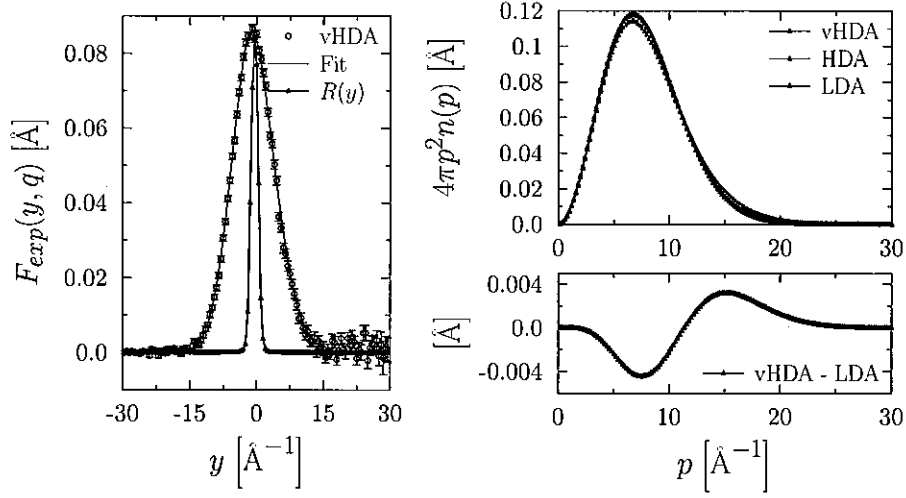


Fig. 15. – Left:  $\bar{F}(y, Q)$  of vHDA at 80 K (blue) together with best fits resulting from the averaged multivariate Gaussian model for the NMD (red) and the angle-averaged instrumental resolution  $\bar{R}(y, Q)$  (grey shadow). Right: radial momentum distribution,  $4\pi p^2 n(p)$ , for LDA (blue), uHDA (green) and vHDA (red). For clarity, error bars are only shown for the vHDA data. The lower right panel shows  $n(p)$  in the region where motions in the O-H stretching direction dominate.

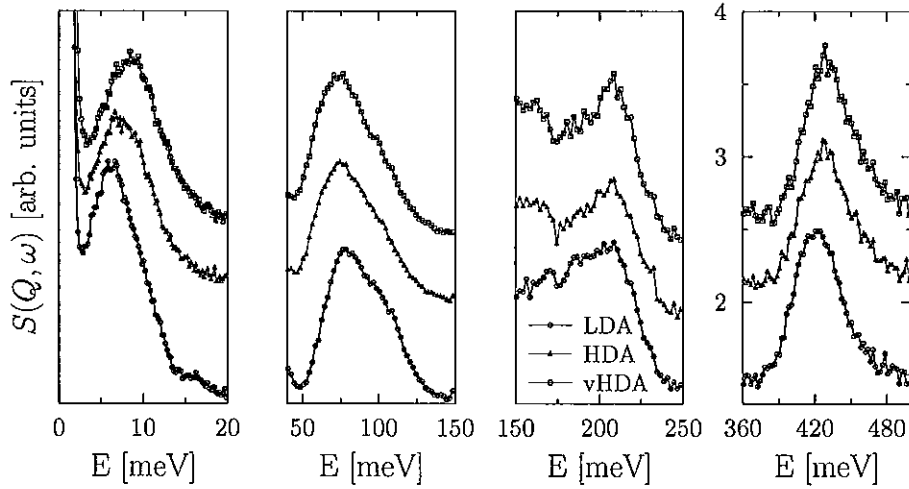


Fig. 16. – INS data for LDA (blue), uHDA (green) and vHDA (red) at 80 K for two distinct incident-neutron energies:  $E_0 = 50$  meV and  $E_0 = 600$  meV. All spectra are shifted vertically for clarity.

from INS within the harmonic assumption [94]. HB can therefore be viewed as the main cause for anharmonicity in amorphous ice. In a novel approach, information from DINS and INS have been used to determine the anharmonicity constants of the O-H stretching modes. These experimental kinetic energies are useful as benchmark values for future PI simulations.



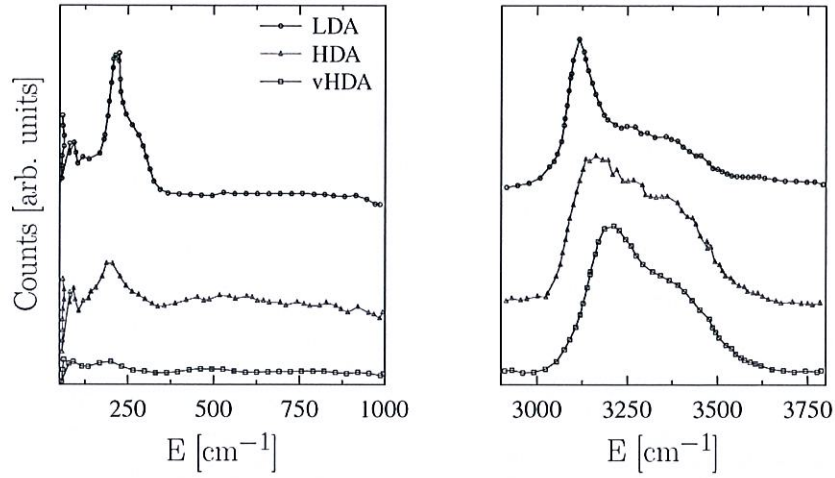


Fig. 17. – Raman spectra of LDA, uHDA and vHDA in the low-frequency and coupled  $\nu(\text{OH})$  stretching region recorded at 80 K. The spectra are normalised with respect to the maximum intensity of the  $\nu(\text{OH})$  feature. The spectra in (a) were normalised by the same factor and these spectra are shown with  $3\times$  magnification. All spectra are shifted vertically for clarity.

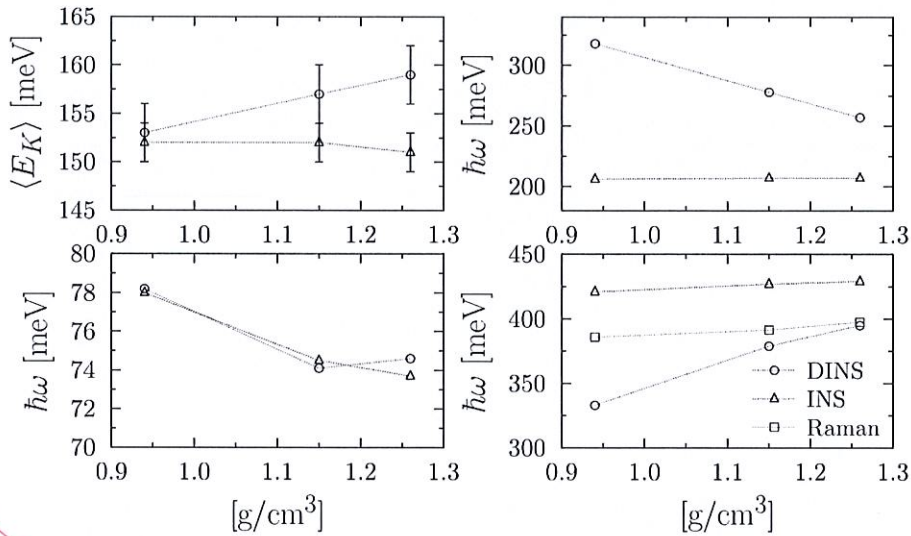


Fig. 18. – Schematic view of the local principal axes associated with hydrogen in the water molecule. (b)  $\langle E_K \rangle$  values from DINS (orange) and corresponding values obtained from INS using the harmonic model introduced in ref. [94, 110] (blue). (c) Energies of the O-H stretching modes,  $\omega_{\text{str}}$ , bending modes,  $\omega_{\text{ben}}$ , and librational modes,  $\omega_{\text{lin}}$ , obtained from INS (blue) and Raman (green), as well as the corresponding values derived from DINS (orange).

The INS spectra for two distinct incident neutron energies,  $E_0 = 50 \text{ meV}$  and  $E_0 = 600 \text{ meV}$ , are shown in fig. 16 in terms of the energy transfer,  $\hbar\omega$ . These data highlight the main inter- and intra-molecular bands: librations or hindered rotations of water molecules at 80 meV, H-O-H bending at 210 meV and O-H stretching at 420 meV. In

*A cosa si riferiscono?  
La figura non ha dei  
labels nei pannelli...*

addition fig. 17 shows the intensity-normalized Raman spectra in the O-H stretching region. From these figures one can appreciate how the position of INS features reflects the average energy of the hydrogen-projected VDoS, whilst the Raman frequencies are associated predominately with coupled in-phase symmetric-stretch motion. The lower values found in the Raman data compared to INS are consistent with what is found for water in the gas phase, *i.e.* the symmetric stretching mode is lower in frequency than the antisymmetric stretching mode [219,220].

#### 4. – Outlook and future directions

This work has presented recent examples of experimental studies of NQEs using DINS, with a particular focus on water systems. As such, it complements recent reviews of electronvolt neutron spectroscopy and its application to an increasingly broad range of challenges in contemporary materials science [32,33]. We have focused our attention on the detailed analysis and interpretation of DINS experiments on water, and specifically on the accurate modelling of H, D, and O NMDs. Specifically, we have shown how the use of multivariate Gaussian functions allows for an meaningful and insightful interpretation of the effects of anharmonicity and anisotropy on the single-particle dynamics of the atomic constituents of water. Also, we have shown how the comparison of DINS observables with the output of state-of-the-art computer simulations can be mutually beneficial. We have also highlighted how DINS is the sole technique capable of providing experimental access to fundamental observables such as NMDs, a quantity that can also be readily obtained from PI simulations. Likewise, the boundaries of the technique have been pushed well beyond recognition, owing to the pressing need for improved sensitivity in order to detect weak fingerprints of anharmonicity and anisotropy in the DINS data.

On the experimental front, we have also explained how the simultaneous and optimal use of cold, thermal, and epithermal neutrons provides a much needed platform for detailed experimental campaigns. In particular, the concurrent use of neutron diffraction along with DINS has proven crucial in order to follow often subtle phase changes in water media. Additionally, seemingly “trivial” neutron transmission measurements over an unprecedentedly broad incident-energy range constitutes the starting point for an accurate data reduction and analysis, as well as a “poor man’s” (yet at the same time very insightful) way of accessing vibrational densities of states. In a similar vein, an increasing number of prompt-gamma activation analysis investigations on VESUVIO is also paving the way for future and exciting experiments where low concentrations of water could be tracked in detail. These additional capabilities offer the exciting prospect of extending the realm of applicability of electronvolt neutron spectroscopy to heavier masses, in addition to the much exploited and inherent ability of DINS to separate the spectroscopic response of H and D.

From a scientific viewpoint, this review has provided a detailed description of the use of DINS to explore water and aqueous systems over the past few years —a success story so far. We do not expect that interest in this important area of science will fade in the foreseeable future, given the plethora of situations of both practical and technological relevance involving this triatom. The use of DINS and INS to probe the fundamental properties of solid, liquid, and supercritical water has been of pivotal importance to test theoretical and computational predictions beyond observables related to structural properties. Substantial efforts in this direction continue in order to find a predictive universal model for water that can account for all of its physico-chemical properties and long list of anomalies [221]. In the context of neutron spectroscopy, fig. 19 summarises

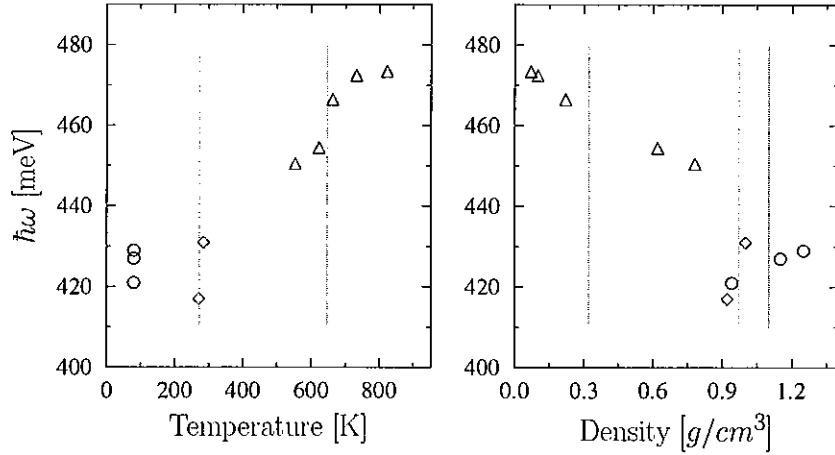


Fig. 19. – Vibrational energies associated with the OH-stretch mode in water as a function of temperature (left) and density (right). Different symbols and colors represent different phases: super critical water at constant pressure (red triangles); amorphous ices at a constant temperature of 80 K (blue circles) [94]; and liquid water and ice across the melting point (green diamonds) [110]. Vertical dotted lines denote the presence of structural changes or phase transitions. Reproduced from ref. [145].

our current knowledge of the way HB in water changes with temperature and density. We have seen in sect. 3 that the primary contribution to  $\langle E_K \rangle$  of the proton in water comes from the ZPE of the OH-stretch vibration. This contribution can be evaluated via integration of the VDOS (obtained from INS or calculations) around those spectral features associated with this mode. A change in their frequencies is a suitable indicator of the overall effects of the HB network on the local potential around the proton, as shown in fig. 19. Whereas the analysis of INS data needs to rely on an underlying physical model, DINS can be used to probe the overall dependence of  $\langle E_K \rangle$  on physical parameters like temperature or pressure, thereby providing stringent benchmarks for detailed theoretical studies. Recent work on amorphous ices has introduced a method to quantify the anharmonicity of atomic motions via the joint use of INS and DINS [94]. From a technological perspective, the data shown in fig. 19 as one enters the supercritical phase from the liquid represent much needed and valuable input into the design of next-generation nuclear-power facilities, given the need for an accurate description of water to enable its use as an efficient moderating material. More recently, this area of work has been extended to concurrent DINS and neutron transmission studies on complex water mixtures [222-224]. Clearly, water has and continues to attract considerable interest across many fields.

One of the major drawbacks of electronvolt neutron spectroscopy can be linked directly to sheer neutron flux. In a recent review [32], we have described in detail emerging possibilities for the development of a next-generation experimental station for *Epithermal and Thermal Neutron Analysis* (ETNA). In what follows, we highlight some of the features that we believe are of most relevance to the scope of the present work. In this context, one of the primary ingredients of ETNA would be the combination of as many different neutron techniques as possible within a single instrument. Some ongoing developments in this direction have been discussed in sect. 2, and have already led to an order-of-magnitude increase in the information content of recent experimental campaigns.

Additional possibilities for ETNA beyond transmission and diffraction capabilities already available on VESUVIO include: the use of  $(n, \gamma)$  nuclear resonances to implement  $\gamma$ -ray Dopplerimetry using neutron resonance capture and neutron resonance transmission analysis for the study of NMDs of much heavier elements such as indium, caesium, gold, tantalum, or silver; the implementation of neutron-energy-resolved prompt-gamma activation techniques for elemental analysis, a capability that will be unique to short-pulse spallation neutron sources; the development of novel detector arrangements (*e.g.*, Debye-Scherrer geometry) to boost the total count rate of DINS measurements by up to two orders of magnitude; and the reduction of backgrounds and spectral congestion with improved detector electronics and incident-beam energy filters. All in all, these developments would pave the way for the widespread use of epithermal neutrons in both fundamental and applied condensed-matter research.

\* \* \*

This work was partially supported within the CNR-STFC Agreement 2014-2020 (N. 3420 2014-2020), concerning collaboration in scientific research at the spallation neutron source ISIS. The authors gratefully acknowledge the UK Science & Technology Facilities Council for financial support and access to beam time at the ISIS Facility.

## REFERENCES

- [1] MARECHAL Y., *The Hydrogen Bond and the Water Molecule: The Physics and Chemistry of Water, Aqueous and Bio-Media* (Elsevier Science) 2006.
- [2] SOPER A. K. and BENMORE C. J., *Phys. Rev. Lett.*, **101** (2008) 065502.
- [3] GAINARU C., AGAPOV A. L., FUENTES-LANDETE V., AMANN-WINKEL K., NELSON H., KSTER K. W., KOLESNIKOV A. I., NOVIKOV V. N., RICHERT R., BHMER R., LOERTING T. and SOKOLOV A. P., *Proc. Natl. Acad. Sci. U.S.A.*, **111** (2014) 49.
- [4] JOHARI G. P., HALLBRUCKER A. and MAYER E., *J. Chem. Phys.*, **92** (1990) 11.
- [5] PRICE D. L., FU L., BERMEJO F. J., FERNANDEZ-ALONSO F. and SABOUNGI M.-L., *Chem. Phys.*, **424** (2013) 62.
- [6] MARKLAND T. E. and BERNE B., *Proc. Natl. Acad. Sci. U.S.A.*, **109** (2012) 21.
- [7] SENESI R., FLAMMINI D., KOLESNIKOV A. I., MURRAY E., GALLI G. and ANDREANI C., *J. Chem. Phys.*, **139** (2013) 074504.
- [8] ANDREANI C., BOSI P., SACCHETTI F. and LOONG C. K., *J. Chem. Phys.*, **83** (1985) 750.
- [9] CERIOTTI M., FANG W., KUSALIK P. G., MCKENZIE R. H., MICHAELIDES A., MORALES M. A. and MARKLAND T. E., *Chem. Rev.*, **116** (2016) 7259.
- [10] MILLER W. H., *Proc. Natl. Acad. Sci. U.S.A.*, **102** (2005) 6660.
- [11] LIN L., MORRONE J. A., CAR R. and PARRINELLO M., *Phys. Rev. B*, **83** (2011) 220302.
- [12] CERIOTTI M. and MANOLOPOULOS D. E., *Phys. Rev. Lett.*, **109** (2012) 100604.
- [13] WIKFELDT K. T., *J. Phys. Conf. Ser.*, **571** (2014) 011012.
- [14] CERIOTTI M., *J. Phys. Conf. Ser.*, **571** (2014) 011011.
- [15] MORRONE J. A. and CAR R., *Phys. Rev. Lett.*, **101** (2008) 017801.
- [16] CERIOTTI M., MICELI G., PIETROPAOLO A., COLOGNESI D., NALE A., CATTI M., BERNASCONI M. and PARRINELLO M., *Phys. Rev. B*, **82** (2010) 174306.
- [17] MARX D. and PARRINELLO M., *Z. Phys. B*, **95** (1994) 143; *J. Chem. Phys.*, **104** (1996) 4077.
- [18] LIN L., MORRONE J. A., CAR R. and PARRINELLO M., *Phys. Rev. Lett.*, **105** (2010) 110602.
- [19] CHENG B., BEHLER J. and CERIOTTI M., *J. Phys. Chem. Lett.*, **7** (2016) 2210.
- [20] FEYNMAN R. P., *Rev. Mod. Phys.*, **20** (1948) 367.

- [21] CAR R. and PARRINELLO M., *Phys. Rev. Lett.*, **55** (1985) 2471.
- [22] SEARS V. F., *Neutron News*, **3** (1992) 3.
- [23] ANDREANI C., DORE J. C. and RICCI F. P., *Rep. Prog. Phys.*, **54** (1991) 731.
- [24] ANDREANI C., CILLOCO F., NENCINI L., ROCCA D. and SINCLAIR R. N., *Mol. Phys.*, **55** (1985) 887.
- [25] ANDREANI C., NARDONE M., RICCI F. P. and SOPER A. K., *Phys. Rev. A*, **46** (1992) 4709.
- [26] ANDREANI C., RICCI M. A., NARDONE M., RICCI F. P. and SOPER A. K., *J. Chem. Phys.*, **107** (1997) 214.
- [27] ANDREANI C., MERLO V., RICCI M. A. and SOPER A. K., *Mol. Phys.*, **73** (1991) 407.
- [28] PARKER S. F., CARLILE C. J., PIKE T., TOMKINSON J., NEWPORT R. J., ANDREANI C., RICCI F. P., SACCHETTI F. and ZOPPI M., *Physica B: Condens. Matter*, **241** (1998) 154.
- [29] GOL'DANSKII V. I., *Sov. Phys. JETP*, **4** (1957) 604.
- [30] IVANOV G. K. and SAYASOV YU. S., *Usp. Fiz. Nauk.*, **90** (1966) 47; *Sov. Phys. Usp.*, **9** (1967) 670.
- [31] ANDREANI C., COLOGNESI D., MAYERS J., REITER G. F. and SENESI R., *Adv. Phys.*, **54** (2005) 377.
- [32] ANDREANI C., KRZYSTYNIAK M., ROMANELLI G., SENESI R. and FERNANDEZ-ALONSO F., *Adv. Phys.*, **66** (2017) 1.
- [33] ANDREANI C., SENESI R., KRZYSTYNIAK M., ROMANELLI G. and FERNANDEZ-ALONSO F., *Exp. Meth. Phys. Sci.*, **49** (2017) 403.
- [34] SILVER R. N. (Editor), *Proceedings of the 1984 Workshop on High Energy Excitations in Condensed Matter* (Los Alamos National Laboratory) 1984, <http://www.osti.gov/scitech/servlets/purl/5858602> (Last accessed 31 August 2016).
- [35] <http://www.isis.stfc.ac.uk> (Last accessed 26 Aug 2016).
- [36] <http://www.isis.stfc.ac.uk/instruments/vesuvio/> (Last accessed 31 August 2016).
- [37] SEEL A. G., KRZYSTYNIAK M. and FERNANDEZ-ALONSO F., *J. Phys. Conf. Ser.*, **571** (2014) 012006.
- [38] SEEL A. G., SENESI R. and FERNANDEZ-ALONSO F., *J. Phys. Conf. Ser.*, **571** (2014) 011001.
- [39] ROMANELLI G., KRZYSTYNIAK M., SENESI R., RASPINO D., BOXALL J., POOLEY D., MOORBY S., SCHOONEVELD E., RHODES N. J., ANDREANI C. and FERNANDEZ-ALONSO F., *Meas. Sci. Technol.*, **28** (2017) 9.
- [40] GUNN J. M. F., ANDREANI C. and MAYERS J., *J. Phys. C: Solid State Phys.*, **19** (1986) L835.
- [41] MAYERS J., EVANS A. C., TIMMS D. L. and COOPER M. J., *Z. Nat. A*, **48** (1993) 425.
- [42] ANDREANI C., PIETROPAOLO A., SENESI R., GORINI G., TARDOCCHI M., BRACCO A., RHODES N. and SCHOONEVELD E. M., *Nucl. Instrum. Methods A*, **481** (2002) 509.
- [43] PIETROPAOLO A., ANDREANI C., D'ANGELO A., SENESI R., GORINI G., IMBERTI S., TARDOCCHI M., RHODES N. and SCHOONEVELD E. M., *Appl. Phys. A*, **74** (2002) 189.
- [44] TARDOCCHI M., PIETROPAOLO A., ANDREANI C., BRACCO A., D'ANGELO A., GORINI G., IMBERTI S., SENESI R., RHODES N. J. and SCHOONEVELD E. M., *Nucl. Instrum. Methods A*, **526** (2004) 477.
- [45] ANDREANI C., D'ANGELO A., GORINI G., IMBERTI S., PIETROPAOLO A., RHODES N. J., SCHOONEVELD E. M., SENESI R. and TARDOCCHI M., *Appl. Phys. A*, **78** (2004) 903.
- [46] GORINI G., PERELLI-CIPPO E., TARDOCCHI M., ANDREANI C., D'ANGELO A., PIETROPAOLO A., SENESI R., IMBERTI S., BRACCO A., PREVITALI E., PESSINA G., RHODES N. J. and SCHOONEVELD E. M., *Nucl. Instrum. Methods A*, **529** (2004) 293.
- [47] IMBERTI S., ANDREANI C., GARBUIO V., GORINI G., PIETROPAOLO A., SENESI R. and TARDOCCHI M., *Nucl. Instrum. Methods A*, **552** (2005) 463.
- [48] SCHOONEVELD E. M., MAYERS J., RHODES N. J., PIETROPAOLO A., ANDREANI C., SENESI R., GORINI G., PERELLI CIPPO E. and TARDOCCHI M., *Rev. Sci. Instrum.*, **77** (2006) 095103.

- [49] PIETROPAOLO A., ANDREANI C., FILABOZZI A., SENESI R., GORINI G., PERELLI CIPPO E., TARDOCCHI M., RHODES N. J. and SCHOONEVELD E. M., *J. Instrum.*, **1** (2006) P04001.
- [50] PIETROPAOLO A., ANDREANI C., FILABOZZI A., PACE E. and SENESI R., *Nucl. Instrum. Methods A*, **570** (2007) 498.
- [51] ANDREANI C., PIETROPAOLO A., SALSANO A., GORINI G., TARDOCCHI M., PACCAGNELLA A., GERARDIN S., FROST C. D., ANSELL S. and PLATT S. P., *Appl. Phys. Lett.*, **92** (2008) 114101.
- [52] PIETROPAOLO A., ANDREANI C., FILABOZZI A., SENESI R., GORINI G., PERELLI-CIPPO E., TARDOCCHI M., RHODES N. J. and SCHOONEVELD E. M., *J. Instrum.*, **1** (2006) P04001.
- [53] PIETROPAOLO A., ANDREANI C., REBAI M., GIACOMELLI L., GORINI G., CIPPO E. P., TARDOCCHI T., FAZZI A., VERONA RINATI G., MARINELLI M., MILANI E., FROST C. D. and SCHOONEVELD E. M., *EPL*, **92** (2010) 68003.
- [54] PIETROPAOLO A. and SENESI R., *Phys. Rep.*, **508** (2011) 45.
- [55] PIETROPAOLO A., ANDREANI C., REBAI M., GIACOMELLI L., GORINI G., PERELLI CIPPO E., TARDOCCHI M., FAZZI A., VERONA RINATI G., VERONA C., MARINELLI M., MILANI E., FROST C. D. and SCHOONEVELD E. M., *EPL*, **94** (2011) 62001.
- [56] REBAI M., ANDREANI C., FAZZI A., FROST C. D., GIACOMELLI L., GORINI G., MILANI E., PERELLI CIPPO E., PIETROPAOLO A., PRESTOPINO G., SCHOONEVELD E., TARDOCCHI M., VERONA C. and VERONA RINATI G., *Nucl. Phys. B*, **215** (2011) 313.
- [57] REBAI M., GIACOMELLI L., ANDREANI C., FAZZI A., FROST C. D., PERELLI CIPPO E., PIETROPAOLO A., RHODES N., TARDOCCHI M., SCHOONEVELD E. and GORINI G., *J. Instrum.*, **7** (2012) C05015.
- [58] GERARDIN S., BAGATIN M., FERRARIO A., PACCAGNELLA A., VISCONTI A., BELTRAMI S., ANDREANI C., GORINI G. and FROST C. D., *IEEE Trans. Device Mat. Re.*, **12** (2012) 437.
- [59] MICELI A., FESTA G., SENESI R., GORINI G. and ANDREANI C., *J. Phys. Conf. Ser.*, **470** (2013) 012001.
- [60] SCHOONEVELD E. M., PIETROPAOLO A., ANDREANI C., PERELLI CIPPO E., RHODES N. J., SENESI R., TARDOCCHI M. and GORINI G., *Rep. Prog. Phys.*, **79** (2016) 094301.
- [61] SENESI R., ANDREANI C., BOWDEN Z., COLOGNESI D., DEGIORGI E., FIELDING A. L., MAYERS J., NARDONE M., NORRIS J., PRAITANO M., RHODES N. J., STIRLING W. G., TOMKINSON J. and UDEN C., *Physica B*, **276-278** (2000) S189.
- [62] MAYERS J., TOMKINSON J., ABDUL-REDAH T., STIRLING W. G., ANDREANI C., SENESI R., NARDONE M., COLOGNESI D. and DEGIORGI E., *Physica B*, **350** (2004) 659.
- [63] MAYERS J. and REITER G., *Meas. Sci. Technol.*, **23** (2012) 045902.
- [64] POSTORINO P., FILLAUX F., MAYERS J., TOMKINSON J. and HOLT R. S., *J. Chem. Phys.*, **94** (1992) 4411; FILLAUX F., BARON M. H., MAYERS J. and TOMKINSON J., *Chem. Phys. Lett.*, **240** (1995) 114.
- [65] EVANS A. C., MAYERS J. and TIMMS D. N., *Phys. Rev. B*, **53** (1996) 3023.
- [66] FIELDING A. L., TIMMS D. N., EVANS A. C. and MAYERS J., *J. Phys.: Condens. Matter*, **8** (1996) 7205.
- [67] MITCHELL P. C. H., GREEN D. A., PAYEN E. and EVANS A. C., *J. Chem. Soc. Faraday Trans.*, **91** (1995) 4467.
- [68] NEMIROVSKY D., MOREH R., ANDERSEN K. H. and MAYERS J., *J. Phys.: Condens. Matter*, **12** (2000) 4293.
- [69] GRAY E. M. A., KEMALI M., MAYERS J. and NORELAND J., *J. Alloys Compounds*, **253** (1997) 291.
- [70] BERMEJO F. J., MOMPEAN F. J., MAYERS J. and EVANS A. C., *Phys. Lett. A*, **189** (1994) 333.
- [71] DAWIDOWSKI J., BERMEJO F. J., BARQUIN L. F., GORRIA P., BARANDARIAN J. M., EVANS A. C. and MAYERS J., *Phys. Lett. A*, **214** (1996) 59.
- [72] MAYERS J., BURKE T. M. and NEWPORT R. J., *J. Phys.: Condens. Matter*, **6** (1994) 641.

- [73] SOSNICK T. R., SNOW W. M., SOKOL P. E. and SILVER R. N., *Europhys. Lett.*, **9** (1989) 707.
- [74] SOSNICK T. R., SNOW W. M. and SOKOL P. E., *Phys. Rev. B*, **41** (1990) 11185.
- [75] SOSNICK T. R., SNOW W. M., SILVER R. N. and SOKOL P. E., *Phys. Rev. B*, **43** (1991) 216.
- [76] ANDREANI C., FILABOZZI A., NARDONE M., RICCI F. P. and MAYERS J., *Phys. Rev. B*, **50** (1994) 12744.
- [77] MAYERS J., BURKE T. M. and NEWPORT R. J., *J. Phys.: Condens. Matter*, **6** (1994) 641.
- [78] DREISMANN C. A., ABDUL-REDAH T., STRERN R. M. F. and MAYERS J., *Phys. Rev. Lett.*, **79** (1997) 2839.
- [79] BAFILE U., ZOPPI M., BAROCCHI F., MAGLI R. and MAYERS J., *Phys. Rev. Lett.*, **75** (1995) 1957.
- [80] BALE U., ZOPPI M., BAROCCHI F., MAGLI R. and MAYERS J., *Phys. Rev. B*, **54** (1996) 11969.
- [81] MAYERS J., ANDREANI C. and COLOGNESI D., *J. Phys.: Condens. Matter*, **9** (1997) 10639.
- [82] NEMIROVSKY D., MOREH R., ANDERSEN K. H. and MAYERS J., *J. Phys.: Condens. Matter*, **11** (1999) 6653.
- [83] NEMIROVSKY D., MOREH R. and KANEKO K., *Surf. Sci.*, **526** (2003) 282.
- [84] MAYERS J., ANDREANI C. and COLOGNESI D., *J. Phys.: Condens. Matter*, **9** (1997) 10639.
- [85] CELLI M., ZOPPI M. and MAYERS J., *Phys. Rev. B*, **58** (1998) 242.
- [86] ANDREANI C., FILABOZZI A. and PACE E., *Phys. Rev. B*, **51** (1995) 8854.
- [87] ANDREANI C., COLOGNESI D., FILABOZZI A., PACE E. and ZOPPI M., *J. Phys.: Condens. Matter*, **10** (1998) 7091.
- [88] ANDREANI C., COLOGNESI D. and PACE E., *Phys. Rev. B*, **60** (1999) 10008.
- [89] KRZYSTYNIK M., ADAMS M. A., LOVELL A., SKIPPER N. T., BENNINGTON S. M., MAYERS J. and FERNANDEZ-ALONSO F., *Faraday Disc.*, **151** (2011) 171.
- [90] KRZYSTYNIK M., *J. Chem. Phys.*, **133** (2010) 144505.
- [91] SEEL A. G., CERIOTTI M. and EDWARDS P. P., *J. Phys.: Condens. Matter*, **24** (2012) 365401.
- [92] ROMANELLI G., CERIOTTI M., MANOLOPOULOS D. E., PANTALEI C., SENESI R. and ANDREANI C., *J. Phys. Chem. Lett.*, **508** (2013) 3251.
- [93] FLAMMINI D., PIETROPAOLO A., SENESI R., ANDREANI C., MCBRIDE F., HODGSON A., ADAMS M. A., LIN L. and CAR R., *J. Chem. Phys.*, **136** (2012) 024504.
- [94] PARMENTIER A., SHEPHARD J. J., ROMANELLI G., SENESI R., SALZMANN C. G. and ANDREANI C., *J. Phys. Chem. Lett.*, **6** (2015) 2038.
- [95] ANDREANI C., ROMANELLI G. and SENESI R., *J. Phys. Chem. Lett.*, **7** (2016) 2216.
- [96] ROMANELLI G., SENESI R., ZHANG X., LOH K. P. and ANDREANI C., *Phys. Chem. Chem. Phys.*, **47** (2015) 31680.
- [97] ROMANELLI G., LISCIO A., SENESI R., ZAMBONI R., TREOSSI E., LISCIO F., GIAMBASTIANI G., PALERMO V., FERNANDEZ-ALONSO F. and ANDREANI C., *Carbon*, **108** (2016) 199.
- [98] KOLESNIKOV A. I., REITER G. F., CHOUDHURY N., PRISK T. R., MAMONTOV E., PODLESNYAK A., EHLERS G., SEEL A. G., WESOŁOWSKI D. J. and ANOVITZ L. M., *Phys. Rev. Lett.*, **116** (2016) 167802.
- [99] KRZYSTYNIK M., DRUŽBICKI K., ROMANELLI G., GUTMANN M. J., RUDIC S., IMBERTI S. and FERNANDEZ-ALONSO F., *Phys. Chem. Chem. Phys.*, **19** (2017) 9064.
- [100] KRZYSTYNIK M., DRUŽBICKI K., and FERNANDEZ-ALONSO F., *Phys. Chem. Chem. Phys.*, **17** (2015) 31287.
- [101] SYRYKH G. F., STOLYAROV A. A., KRZYSTYNIK M., ROMANELLI G. and SADYKOV R. A., *JETP Lett.*, **105** (2017) 591.

- [102] TIAN K. V., YANG B., YUE Y., BOWRON D. T., MAYERS J., DONNAN R. S., DOBO NAGY C., NICHOLSON J. W., FANG D. C., LINDSAY GREER A., CHASS G. A. and GREAVES G. N., *Nat. Commun.*, **6** (2015) 8631.
- [103] GORINI G., for the Ancient Charm collaboration, *Nuovo Cimento C*, **30** (2007) 47.
- [104] KASZTOVSZKY Zs., KIS Z., BELGYA T., KOCKELMANN W., IMBERTI S., FESTA G., FILABOZZI A., ANDREANI C., KIRFEL A., BIR K., Dzs K., HAJNAL Zs., KUDEJOVA P. and TARDOCCHI M., *J. Radioanal. Nucl. Chem.*, **278** (2008) 661; 751.
- [105] PERELLI CIPPO E., BORELLA A., GORINI G., KOCKELMANN W., MOXON M., POSTMA H., RHODES N. J., SCHILLEBEECK P., SCHOONENVELD E. M., TARDOCCHI M., DUSZ K., HAJNAL Z., BIRO K., PORCINAI S., ANDREANI C. and FESTA G., *J. Anal. At. Spectrosc.*, **J26** (2011) 992.
- [106] ANDREANI C., PIETROPAOLO A., SALSANO A., GORINI G., TARDOCCHI M., PACCAGNELLA A., GERARDIN S., FROST C. D., ANSELL S. and PLATT S. P., *Appl. Phys. Lett.*, **92** (2008) 114101.
- [107] BEDOGNI R., ESPOSITO A., ANDREANI C., SENESI R., DE PASCALE M. P., PICOZZA P. G., PIETROPAOLO A., GORINI G., FROST C. D. and ANSELL S., *Nucl. Instrum. Methods Phys. Res. A*, **612** (2009) 143.
- [108] HOHENBERG P. C. and PLATZMANN P. M., *Phys. Rev.*, **152** (1966) 198.
- [109] SENESI R., ROMANELLI G., ADAMS M. A. and ANDREANI C., *Chem. Phys.*, **427** (2013) 111.
- [110] ANDREANI C., ROMANELLI G. and SENESI R., *Chem. Phys.*, **427** (2013) 106.
- [111] PARMENTIER A., ANDREANI C., ROMANELLI G., SHEPHARD J. J., SALZMANN C. G. and SENESI R., *Frontiers Phys.*, **13** (2018) 136101.
- [112] PIETROPAOLO A., SENESI R., ANDREANI C., BOTTI A., RICCI M. A. and BRUNI F., *Phys. Rev. Lett.*, **100** (2008) 127802.
- [113] PANTALEI C., PIETROPAOLO A., SENESI R., ANDREANI C., IMBERTI S., MAYERS J., BURNHAM C. and REITER G., *Phys. Rev. Lett.*, **100** (2008) 177801.
- [114] REITER G. F. and SILVER R., *Phys. Rev. Lett.*, **54** (1985) 1047.
- [115] WATSON G., *J. Phys.: Condens. Matter*, **8** (1996) 5955.
- [116] FERNANDEZ-ALONSO F. and PRICE D. L. (Editors), *Neutron Scattering – Fundamentals* (Academic Press, New York) 2013.
- [117] WINDSOR C. G., *Pulsed Neutron Scattering* (Taylor and Francis, London) 1981.
- [118] LOVESEY S. W., *Theory of Neutron Scattering from Condensed Matter* (Oxford University Press, Oxford) 1987.
- [119] WEST G. B., *Phys. Rev. C*, **18** (1975) 263.
- [120] PACE E., SALMÈ G. and WEST G., *Phys. Lett. B*, **273** (1991) 3.
- [121] MAYERS J., ANDREANI C. and BACIOCCO G., *Phys. Rev. B*, **39** (1989) 2022.
- [122] GERSCH H. A. and RODRIGUEZ L. J., *Phys. Rev. A*, **8** (1973) 905.
- [123] RODRIGUEZ L. J., GERSCH H. A. and MOOK H., *Phys. Rev. A*, **9** (1974) 2085.
- [124] SEARS V. F., *Phys. Rev. B*, **30** (1984) 44.
- [125] SILVER R. N. and REITER G. F., *Phys. Rev. B*, **35** (1987) 3647.
- [126] SILVER R. N., *Phys. Rev. B*, **37** (1988) 3794; *Phys. Rev. B*, **39** (1989) 4022.
- [127] CARRARO C. and KOONIN S. E., *Phys. Rev. Lett.*, **65** (1990) 2792.
- [128] MAZZANTI F., BORONAT J. and POLLS A., *Phys. Rev. B*, **53** (1996) 5661.
- [129] GLYDE H. R., AZUAH R. T. and STIRLING W. G., *Phys. Rev. B*, **62** (2000) 14337 and references therein.
- [130] PACE E., SALMÈ G. and RINAT A., *Phys. Lett. B*, **325** (1994) 289.
- [131] AMBROSEK D., CHATZIDIMITRIOU-DREISMANN C. A., KRAUSE P., MANZ J., NAUMANN H. and VAN WÜLLEN C., *Chem. Phys.*, **302** (2004) 229.
- [132] NEWTON R., *Scattering Theory of Waves and Particles* (Springer, Berlin) 1982, p. 606.
- [133] GUNN J. M. F. and WARNER M., *Z. Phys. B Condens. Matter*, **56** (1984) 1.
- [134] DATTA GUPTA S. and REITER G. F., *Phys. Rev. A*, **31** (1985) 1074.
- [135] WEINSTEIN J. and NEGELE J. W., *Phys. Rev. Lett.*, **49** (1982) 1016.
- [136] REITER G. F. and BECHER T., *Phys. Rev. B*, **32** (1985) 4492.
- [137] GERSCH H. A., RODRIGUEZ L. J. and SMITH P. N., *Phys. Rev. A*, **5** (1972) 1547.



- [138] SEARS V. F., *Phys. Rev. B*, **30** (1984) 44.
- [139] SEARS V. F., SVENSSON E. C., MARTEL P. and WOODS A. D. B., *Phys. Rev. Lett.*, **49** (1982) 279.
- [140] REITER G. F., MAYERS J. and NORELAND J., *Phys. Rev. B*, **65** (2002) 104305.
- [141] SENESI R., *Nucl. Instrum. Methods A*, **661** (2012) 70.
- [142] SENESI R., FLAMMINI D., ROMANELLI G. and ANDREANI C., *Nucl. Instrum. Methods A*, **704** (2013) 36.
- [143] ANDREANI C., DEGIORGI E., SENESI R., CILLOCO F., COLOGNESI D., MAYERS J., NARDONE M. and PACE E., *J. Chem. Phys.*, **114** (2001) 387.
- [144] ROMANELLI G., FERNANDEZ-ALONSO F. and ANDREANI C., *J. Phys. Conf. Ser.*, **571** (2014) 012003.
- [145] ROMANELLI G., PhD Thesis, Università degli Studi di Roma-Tor Vergata, (2015).
- [146] ROMANELLI G. and KRZYSTYNIK M., *Nucl. Instrum. Methods A*, **819** (2016) 84.
- [147] HERZBERG G., *Molecular Spectra and Molecular Structure* (Krieger Publishing Co., Malabar) 1989.
- [148] SIVARDIERE J., *Am. J. Phys.*, **54** (1986) 12.
- [149] KRZYSTYNIK M., *Phys. Rev. B*, **82** (2010) 064301.
- [150] KRZYSTYNIK M. and FERNANDEZ-ALONSO F., *Phys. Rev. B*, **83** (2011) 134305.
- [151] MOREH R. and NEMIROVSKY D., *Radiat. Phys. Chem.*, **61** (2001) 557.
- [152] HUANG K., *Statistical Mechanics* (John Wiley, New York) 1987.
- [153] MARADUDIN A. A., MONTROLL E. W., WEISS G. I. and IPATOVA I. P., *Theory of Lattice Dynamics in the Harmonic Approximation* (Academic Press, New York) 1971.
- [154] BECK T. L., in *Free Energy Calculations – Theory and Applications in Chemistry and Biology*, edited by CHIPOT CH. and POHORILLE A. (Springer-Verlag, Berlin) 2007, pp. 387–420.
- [155] BARONI S., DE GIRONCOLI S., DAL CORSO A. and GIANNOZZI P., *Rev. Mod. Phys.*, **73** (2001) 515.
- [156] LIU J., ANDINO R. S., MILLER C. M., CHEN X., WILKINS D. M., CERIOTTI M. and MANOLOPOULOS D. E., *J. Phys. Chem. C*, **117** (2013) 2944.
- [157] BERNE B. J. and THIRUMALAI D., *Annu. Rev. Phys. Chem.*, **37** (1986) 401.
- [158] CERIOTTI M., MORE J. and MANOLOPOULOS D. E., *Comput. Phys. Commun.*, **185** (2014) 1019.
- [159] CEPERLEY D. M., *Rev. Mod. Phys.*, **67** (1995) 279.
- [160] HABERSHON S., MANOLOPOULOS D. E., MARKLAND T. E. and MILLER III T. F., *Annu. Rev. Phys. Chem.*, **64** (2013) 387.
- [161] MORRONE J. A. et al., *J. Chem. Phys.*, **126** (2007) 234504.
- [162] <http://flnph.jinr.ru/en/> (Last accessed on February 2018).
- [163] <https://www.psi.ch/sinq/> (Last accessed on February 2018).
- [164] SENESI R., KOLESNIKOV A. I. and ANDREANI C., *J. Phys. Conf. Ser.*, **571** (2014) 012007.
- [165] IMBERTI S., ANDREANI C., GARBUIO V., GORINI G., PIETROPAOLO A., SENESI R. and TARDOCCI M., *Nucl. Instrum. Methods A*, **552** (2005) 463.
- [166] SEEL A. G., SARTBAEVA A., MAYERS J., RAMIREZ-CUESTA A. J. and EDWARDS P. P., *J. Chem. Phys.*, **134** (2011) 114511.
- [167] KRZYSTYNIK M., RICHARDS S. E., SEEL A. G. and FERNANDEZ-ALONSO F., *Phys. Rev. B*, **88** (2013) 184304.
- [168] KRZYSTYNIK M., SEEL A. G., RICHARDS S. E., GUTMANN M. J. and FERNANDEZ-ALONSO F., *J. Phys. Conf. Ser.*, **571** (2014) 012009.
- [169] MAYERS J. and ADAMS M. A., *Nucl. Instrum. Methods A*, **625** (2011) 47.
- [170] EVANS A. C., MAYERS J., TIMMS D. N. and COOPER M. J., *Z. Naturforsch A: Phys. Sci.*, **48** (1993) 425.
- [171] NEWPORT R. J., PAOLI M. P., PUGH V. T., SINCLAIR R. N., TAYLOR A. D. and WILLIAMS W. G., *Proceedings of the Eighth Meeting of the International Collaboration on Advanced Neutron Sources (ICANS VIII)*, Rutherford Appleton Laboratory Report No. RAL-TR-85-110 (Chilton) 1985, p. 562.

- [172] SEEGER P. A., TAYLOR A. D. and BRUGGER R. M., *Nucl. Instrum. Methods A*, **240** (1985) 98.
- [173] ANDREANI C., COLOGNESI D., DEGIORGI E., FILABOZZI A., NARDONE M., PACE E., PIETROPAOLO A. and SENESI R., *Nucl. Instrum. Methods A*, **497** (2003) 535.
- [174] GIACOMELLI L., ANDREANI C., FAZZI A., FROST C. D., GORINI G., PERELLI CIPPO E., PIETROPAOLO A., REBAI M., SCHUHMACHER H., TARDOCCHI M., VERONA C., VERONA RINATI G. and ZIMBAL A., *J. Nucl. Phys. B Proc. Suppl.*, **215** (2011) 242.
- [175] PIETROPAOLO A., TARDOCCHI M., SCHOONEVELD E. M. and SENESI R., *Nucl. Instrum. Methods A*, **568** (2006) 826.
- [176] PIETROPAOLO A., PERELLI CIPPO E., GORINI G., TARDOCCHI M., SCHOONEVELD E. M., ANDREANI C. and SENESI R., *Nucl. Instrum. Methods A*, **608** (2009) 121.
- [177] MICELI A., FESTA G., SENESI R., PERELLI CIPPO E., GIACOMELLI L., TARDOCCHI M., SCHERILLO A., SCHOONEVELD E., FROST C., GORINI G. and ANDREANI C., *J. Anal. At. Spectrom.*, **29** (2014) 1897.
- [178] FERMI E., *Nuovo Cimento (1924-1942)*, **13** (1936) 9.
- [179] RODRÍGUEZ PALOMINO L. A., DAWIDOWSKI J., MÁRQUEZ DAMIÁN J. I., CUELLO G. J., ROMANELLI G. and KRZYSTYNIAN M., *Nucl. Instrum. Methods A*, **870** (2017) 84.
- [180] ROMANELLI G., RUDIC S., ZANETTI M., KRZYSTYNIAN M., GORINI G., ANDREANI C., FERNANDEZ-ALONSO F. and SKORO G., *Nucl. Instrum. Methods A*, **888** (2018) 88.
- [181] COLOGNESI D., PIETROPAOLO A., SENESI R. and RAMIREZ-CUESTA A. J., *Phys. Rev. B*, **76** (2007) 174206.
- [182] SENESI R., COLOGNESI D., PIETROPAOLO A. and ABDUL-REDAH T., *Phys. Rev. B*, **72** (2005) 054119.
- [183] SIVIA D., *Data Analysis: A Bayesian Tutorial* (Clarendon Press, Oxford) 1996.
- [184] FU L., VILLETTE S., PETOUD S., FERNANDEZ-ALONSO F. and SABOUNGI M.-L., *J. Phys. Chem. B*, **115** (2011) 1881.
- [185] PRICE D. L., FU L., BERMEJO F. J., FERNANDEZ-ALONSO F. and SABOUNGI M.-L., *Chem. Phys.*, **424** (2013) 62.
- [186] LI J. C., *J. Chem. Phys.*, **105** (1996) 6733; REITER G. F., LI J. C., MAYERS J., ABDUL REDAH T. and PLATZMAN P., *Braz. J. Phys.*, **34** (2004) 142.
- [187] ANDREANI C., COLOGNESI D., DEGIORGI E. and RICCI M. A., *J. Chem. Phys.*, **115** (2001) 11243.
- [188] PIETROPAOLO A., SENESI R., ANDREANI C., BOTTI A., RICCI M. A. and BRUNI F., *Phys. Rev. Lett.*, **100** (2008) 127802.
- [189] PIETROPAOLO A., SENESI R., ANDREANI C., BOTTI A., RICCI M. A. and BRUNI F., *Phys. Rev. Lett.*, **103** (2009) 069802.
- [190] PIETROPAOLO A., SENESI R., ANDREANI C. and MAYERS J., *Braz. J. Phys.*, **39** (2009) 318 and references therein.
- [191] FLAMMINI D., RICCI M. A. and BRUNI F., *J. Chem. Phys.*, **130** (2009) 236101.
- [192] GARBUIO V., ANDREANI C., IMBERTI S., PIETROPAOLO A., REITER G. F., SENESI R. and RICCI M. A., *J. Chem. Phys.*, **127** (2007) 4501.
- [193] REITER G., BURNHAM C., HOMOUZ D., PLATZMAN P. M., MAYERS J., ABDUL-REDAH T., MORAVSKY A. P., LI J. C., LOONG C.-K. and KOLESNIKOV A. I., *Phys. Rev. Lett.*, **97** (2006) 247801.
- [194] YOKOYAMA H., KANNAMI M. and KANNO H., *Chem. Phys. Lett.*, **463** (2008) 99.
- [195] HOMOUZ D., REITER G., ECKERT J., MAYERS J. and BLINC R., *Phys. Rev. Lett.*, **98** (2007) 115502.
- [196] BURNHAM C. J., ANICK D. J., MANKOO P. K. and REITER G. F., *J. Chem. Phys.*, **128** (2008) 154519.
- [197] MORRONE J. A., SRINIVASAN V., SEBASTIANI D. and CAR R., *J. Chem. Phys.*, **126** (2007) 234504.
- [198] MORRONE J., LIN L. and CAR R., *J. Chem. Phys.*, **130** (2009) 204511.
- [199] HABERSHON S., MARKLAND T. E. and MANOLOPOULOS D. E., *Chem. Phys.*, **131** (2019) 24501.
- [200] FINKELSTEIN Y. and MOREH R., *Chem. Phys.*, **431** (2014) 58.

- [201] BYRD A. J., PANT K. K. and GUPTA R. B., *Ind. Eng. Chem. Res.*, **42** (2007) 3574.
- [202] CABANAS A., LI J., BLOOD P., CHUDOKA T., LOJKOWSKI W., POLIAKOFF M. and LESTER E., *J. Supercrit. Fluids*, **40** (2007) 284.
- [203] OKA Y. *et al.*, *Super Light Water Reactors and Super Fast Reactors* (Springer, Berlin) 2010.
- [204] FANG ZHEN, *Rapid production of Micro- and Nano-particles using Supercritical Water* (Springer, Berlin) 2010.
- [205] GALLI G. and PAN D., *Proc. Natl. Acad. Sci. U.S.A.*, **110** (2013) 6250.
- [206] BURNHAM C. J., REITER G. F., MAYERS J., ABDUL-REDAH T., REICHERT H. and DOSCH H., *Phys. Chem. Chem. Phys.*, **8** (2006) 3966.
- [207] BURNHAM C. J., HAYASHI T., NAPOLEON R. L., KEYES T., MUKAMEL S. and REITER G. F., *J. Chem. Phys.*, **135** (2011) 144502.
- [208] SENESI R., ROMANELLI G., ADAMS M. A. and ANDREANI C., *Chem. Phys.*, **427** (2013) 111.
- [209] MOREH R. and NEMIROVSKY D., *J. Chem. Phys.*, **133** (2010) 084506.
- [210] SOPER A. K., *J. Phys. Chem. B*, **115** (2011) 14014.
- [211] SOPER A. K., *Chem. Phys.*, **258** (2000) 121.
- [212] ANDREANI C. *et al.*, paper in preparation 2018.
- [213] LI X. Z., WALKER B. and MICHAELIDES A., *Proc. Natl. Acad. Sci. U.S.A.*, **108** (2011) 6369.
- [214] MARKLAND T. E. and BERNE B. J., *Proc. Natl. Acad. Sci. U.S.A.*, **109** (2012) 7988.
- [215] FALENTY A., HANSEN T. C. and KUHS W. F., *Nature*, **516** (2014) 231.
- [216] SALZMANN C. G., RADAELLI P. G., SLATER B. and FINNEY J. L., *Phys. Chem. Chem. Phys.*, **13** (2011) 18468.
- [217] LOERTING T., WINKEL K., SEIDL M., BAUER M., MITTERDORFER C., HANDLE P. H., SALZMANN C. G., MAYER E., FINNEY J. L. and BOWRON D. T., *Phys. Chem. Chem. Phys.*, **13** (2011) 8783.
- [218] LOERTING T., SALZMANN C. G., KOHL I., MAYER E. and HALLBRUCKER A. A., *Phys. Chem. Chem. Phys.*, **3** (2001) 5355.
- [219] BERNATH P. F., *Phys. Chem. Chem. Phys.*, **4** (2002) 1501.
- [220] TENNYSON J., BERNATH P. F., BROWN L. R., CAMPARGUE A., CSSZR A. G., DAUMONT L., GAMACHE R. R., HODGES J. T., NAUMENKO O. V., POLYANSKY O. L., ROTHMAN L. S., VANDAELE A. C. and ZOBOV N. F., *Pure Appl. Chem.*, **86** (2014) 71.
- [221] PAESANI F., *Acc. Chem. Res.*, **49** (2016) 1844.
- [222] GRANADA J. R., MAYER R. E., DAWIDOWSKI J., SANTISTEBAN J. R., CANTARGI F., BLOSTEIN J. J., RODRÍGUEZ PALOMINO L. A. and TARTAGLIONE A., *Eur. Phys. J. Plus*, **131** (2016) 216.
- [223] RODRÍGUEZ PALOMINO L. A., BLOSTEIN J. J. and DAWIDOWSKI J., *J. Instrum.*, **8** (2013) P08016.
- [224] RODRÍGUEZ PALOMINO L. A., BLOSTEIN J. J. and DAWIDOWSKI J., *Nucl. Instrum. Methods A*, **646** (2011) 142.